LAWRENCE
LIVERMORE
NATIONAL
LABORATORY

UCRL-TR-211695

59Fe(n,g)60Fe and 60Fe(n,g)61Fe Reaction Rates from Local Systematics

K. Kelley, R. D. Hoffman, M. Drake

April 26, 2005

This work was performed under the auspices of the U.S. Department of Energy by University of California, Lawrence Livermore National Laboratory under Contract W-7405-Eng-48.

UCRL-TR-211695

^{59}Fe(n,γ)^{60}Fe and ^{60}Fe(n,γ)^{61}Fe Reaction Rates from Local Systematics

K. Kelley[1], R. D. Hoffman, and M. Drake[2]
Nuclear Theory and Modeling Group
Physics and Advanced Technologies, N-Division
Lawrence Livermore National Laboratory
Livermore, CA 94550
kelley24@llnl.gov

ABSTRACT

We present modeled neutron capture cross sections relevant to stellar production of ^{60}Fe. Systematics for the input parameters required by the Hauser-Feshbach statistical model are developed based on measured data in the local region of the isotopic plane ($20 \leq Z \leq 29$, $43 \leq A \leq 65$). These parameters and used to calculate reaction cross sections and rates for select target isotopes. Modeled cross sections are compared to experimental data where available. The ^{59}Fe(n,γ)^{60}Fe and ^{60}Fe(n,γ)^{61}Fe rates are compared to previous calculations. A brief discussion of errors related to the modeling is provided. We conclude by investigating the sensitivity of stellar production of ^{26}Al and ^{60}Fe to the ^{59}Fe(n,γ)^{60}Fe and ^{60}Fe(n,γ)^{61}Fe reaction rates using a single zone model.

Subject headings: nuclear reactions, nucleosynthesis, abundances - stars: interiors - supernovae: general

1. Introduction

The radioactive nucleus ^{60}Fe has long been an elusive candidate for γ-ray line study in the interstellar medium. With a decay half life $\tau_{1/2} = 1.5\times10^6$ years, any ^{60}Fe produced in pre- and post-supernovae processes will remain in the interstellar medium long enough that its γ-ray flux should, in principle, be observable even when the period between supernovae is long. The observability of the gamma ray flux is, of course, dependent on the amount of ^{60}Fe produced and the sensitivity of the detector.

The synthesis of ^{60}Fe has been closely tied to that of ^{26}Al ($\tau_{1/2} = 7.17 \times 10^5$ years) (Timmes *et al.* 1995), which has been observed in the Galactic plane (Hartmann, Diel, etc). Based on theoretical predictions of stellar yields (Woosley & Weaver 1995) and a coordinated survey of galactic chemical evolution (Timmes Woosley & Weaver 1995), $\sim$ 2 $M_\odot$ of ^{26}Al was predicted to exist in steady state in the Galaxy. The expected line-flux ratio of ^{60}Fe/^{26}Al (for each of the two lines of ^{60}Fe) was predicted to be 0.16 if SNII are the only sources of ^{26}Al in the Galaxy. Such a flux was well below the threshold detection limits of the orbiting γ-ray telescopes in the 1990's. Recently, detection of both ^{26}Al and ^{60}Fe with the RHESSI satellite has been reported (Smith 2003) initially with a flux ratio of 0.16, in agreement with the prediction. The values has since been revised to 0.093 (Smith 2004). This latter result is confirmed by initial measurements

[1]Department of Physics, University of California, Davis Davis, CA 95616

[2]United States Naval Academy, Annapolis, MD

from the INTEGRAL satellite which put the flux ratio at 0.11 ± 0.03 (Harris 2005).

However, recent improvements to the stellar model and the nuclear reaction rate library used in the 1995 survey (Rauscher *et al.* 2002) now indicate more ^{60}Fe production by roughly a factor two in a solar metallicity 25 $M_\odot$ star. In addition, the amount of predicted ^{26}Al has also changed, bringing into question the amount of both radionucleides ascribed to synthesis in massive stars (Prantzos 2004).

There are several factors that affect the synthesis of ^{60}Fe. Previous studies suggest that both pre- and post-explosive processing contribute (Timmes *et al.* 1995). Most of it is made in a high temperature helium burning shell just prior to collapse. The most important nuclear reaction uncertainties are the neutron capture rate for ^{59}Fe (less so ^{60}Fe), and the weak decay rates of ^{60}Fe and ^{60}Co. Other important rates are those that produce neutrons during the $s-$process, such as ^{22}Ne(α,n)^{25}Mg, and of course ^{12}C(α,γ)^{16}O which affects the size of the helium shell.

Possibly more important are the roles of stellar convection and mass loss. The latter was not included in the calculation of the stellar yields in (Woosley & Weaver 1995) . In this paper we will investigate the uncertainties in the neutron catpure rates of ^{59,60}Fe, leaving the other items for future study.

Since no experimental capture cross sections exist for these radionuclides theoretical modeling techniques must be employed. We will concentrate on comparisons of our statistical model input quantities and calculated capture cross sections to those previously developed by (Woosley *et al.* 1975; Holmes *et al.* 1976), hereafter WFHZ, and (Rauscher & Thielemann 2000; Rauscher & Thielemann 2001), hereafter RT, used to calculate the stellar yields used in the 1995 GCE study (Timmes Woosley & Weaver 1995) and the most recent nucleosynthesis (Rauscher *et al.* 2002) respectively. For a summary of the cross section development and a detailed sensitivity study of nucleosynthesis in massive stars using WFHZ vs. RT reaction rates, see (Hoffman *et al.* 1999). For an online library of the rates used in both studies, see (Hoffman *et al.* 2002).

Section 2 details how the input parameters for the Hauser-Feshbach statistical model were developed. Section 4 gives results and comparisons to experimental data and to previous calculations. We explore sensitivity to the statistical model input quantities in section 5. In section 6 we investigate the effect our modeled ^{59}Fe(n,γ)^{60}Fe and ^{60}Fe(n,γ)^{61}Fe have on nucleosynthesis. Conclusions follow.

2. Statistical Model Input Parameters

Both direct and compound nuclear processes contribute to neutron capture reactions. However, at the incident energies of interest in this study, direct capture accounts for only a small fraction of the cross section, and may be omitted. We model our cross sections in the context of the Hauser-Feshbach model (Hauser & Feshbach 1952), where the cross section is given in terms of energy-averaged transmission functions. Consider the reaction involving target $\mathcal{I}$ in state μ and incident particle j resulting in a residual $\mathcal{L}$ in state ν and outgoing particle(s) k. For reactions with particles in the exit channel, the cross section is given by

$$\bar{\sigma}_{jk}^{\mu\nu}(E) = \frac{\pi\lambda\!\!\!^{-2}_j}{g_\mu g_j} \times \sum_{i,i',l,l',J,\Pi} g_J T_{jil}^{J\Pi}(E) \frac{T_{ki'l'}^{J\Pi}(E+Q_{jk}^{\mu\nu})}{T_{tot}}. \quad (1)$$

For radiative capture, the cross section is given by

$$\bar{\sigma}_{j\gamma}^{\mu\nu}(E) = \frac{\pi\lambda\!\!\!^{-2}_j}{g_\mu g_j} \sum_{i,l,X,L,J,\Pi} g_J T_{jil}^{J\Pi}(E) \frac{T_{\gamma XL}^{J\Pi}(\epsilon_\gamma^\nu)}{T_{tot}}. \quad (2)$$

In these expressions, $\pi\lambda\!\!\!^{-2}_j = 0.6566(\hat{A}_j E_j^\mu)^{-1}$ barns, with $\hat{A}_j = (A_I A_j)/(A_I + A_j)$ being the reduced mass in atomic mass units and E_j^μ is the center of mass energy in units of MeV. The g_i are statistical weights, given by $g_i = 2J_i + 1$. $Q_{jk}^{\mu\nu}$ is the Q-value for the reaction, and the T are transmission coefficients. The sum extends over channel spins i, partial waves l, and spins J and parities Π of accessible exited compound nuclear states. For photons, the partial waves are replaced by multipolarities. The denominator T_{tot} in Equations 1 and 2 represents the sum of the transmission probability to all accessible exit

channels, given by

$$T_{tot} = \sum_{k'',i'',l''} \left[\sum_{\nu''=0}^{\omega} T^{J\Pi}_{k''i''l''}(E^{\nu''}) + \sum_{J'\Pi'} \int_{E_\omega}^{E_{max}} T^{J\Pi}_{k''i''l''}(\epsilon)\rho(E^{k''}_{exc} - \epsilon, J', \Pi')d\epsilon \right] + \sum_{X'',L''} \left[\sum_{\nu''=0}^{\omega} T^{J\Pi}_{\gamma X''L''}(\epsilon^{\nu''}_{\gamma}) + \sum_{J'\Pi'} \int_{0}^{\epsilon^{\omega}_{\gamma}} T^{J\Pi}_{\gamma X''L''}(\epsilon)\rho(E^{\gamma}_{exc} - \epsilon, J', \Pi')d\epsilon \right]. \quad (3)$$

In this expression, $\rho(E, J, \Pi)$ is the spin dependent level density, ω is the highest level up to which the level scheme is complete, E_{max} is the maximum excitation energy available, and $E^{k''}_{exc}$ is the excitation energy for the channel k''.

The laboratory cross section, where the target is in the ground state and excited states in the residual cannot be distiguished, is given as the sum of Equations 1 and 2 over the residual state ν, i.e.

$$\bar{\sigma}^{lab}_{jk} = \sum_{\nu} \bar{\sigma}^{0\nu}_{jk}. \quad (4)$$

This is the quantity that is measured in the laboratory and is of use in comparing to experimental cross section data.

Reaction rates λ_{jk} are determined by convolution of the cross section with a maxwellian velocity distribution, which yields

$$\lambda_{jk} = N_A \langle \sigma v \rangle_{jk} = \sqrt{\frac{8}{\pi \mu_j}} \frac{N_A}{(k_B T)^{3/2}} \int_0^{\infty} \bar{\sigma}_{jk} E_j \exp(-E_j/k_B T) dE_j. \quad (5)$$

Here, j and k refer to the projectile and outgoing particle, respectively. The reduced mass of the projectile is denoted by μ_j, and N_A and k_B are Avagadro's number and the Boltzmann constant. It is generally more useful to express this quantity in terms of billions of degrees Kelvin (T_9):

$$\lambda_{jk} = \frac{3.732 \times 10^{10}}{\hat{A}_j^{1/2} T_9^{3/2}} \int_0^{\infty} \sigma_{jk} E_j \exp(-11.605\ E_j/T_9) dE_j \ \mathrm{cm^3 mol^{-1} sec^{-1}} \quad (6)$$

where $\hat{A}_j$ is the reduced mass of the projectile in atomic units.

Our cross section calculations include the Moldauer approximation for the width fluctuation correction (Moldauer 1976), and a simple exciton model for pre-equilibrium emission (Cline & Blann 1971). Pre-compound emission rates for nucleons and alpha particles are determined in accordance with (Gadioli *et al.* 1973) and (Milazzo-Colli & Braga-Marcazzan 1973), respectively. Pre-equilibrium emission only becomes significant in this isoptopic region for incident neutron energies above ∼5 MeV, and hence will not affect neutron capture. To carry out statistical model calculations, we adopt the STAPRE code (Uhl & Strohmaier 1976), which embodies these treatments. We have modified this code to enable the use of additional prescriptions for the relevant nuclear physics inputs, primarily the photon transmission coefficients and the level densities.

In this section, we discuss the important ingredients of statistical model calculations and the methods utilized to estimate them. These include the requisite nuclear structure data (energies, spins, and parities of the ground states and all known excited states, as well as detailed branching ratios for gamma-cascade from excited to low-lying states), particle and photon transmission coefficients, and nuclear level densities. The reliability of Hauser-Feshbach calculations is chiefly determined by the accuracy with which these components can be evaluated.

2.1. Nuclear Structure Data

We adopt the experimental mass excess values of (Wapstra *et al.* 2003) in determining nuclear binding and separation energies. These quantites are needed in calculating excitation energies and Q-values. Ground state spin and parity assignments are from the Evaluated Nuclear Structure Data File (ENSDF 2003). The nuclear structure data needed to model gamma-ray cascades are taken from the level schemes and parameters found in the second Reference Input Parameter Library (RIPL). For the iron, cobalt, and nickel isotopes, additional evaluation was performed by

R. Bauer (Bauer 2002). In general, we use several more levels than were available in the previous cross section calculations of WFHZ and RT.

2.2. Nuclear Level Densities

For excitation energies at the neutron binding energy and above, we adopt a back-shifted Fermi gas formulation of the nuclear level density (Gilbert & Cameron 1965):

$$\rho(U,J) = \rho(U)\ f(U,J) \tag{7}$$

where $\rho(U)$ is the state density, $U = E - \Delta$ is the back-shifted energy, and J is the spin of the compound nucleus. We assume an equal distribution of parity states, so that $\rho(U,J,\Pi) = \frac{1}{2}\rho(U,J)$. The state density and spin dependence are given by

$$\rho(U) = \frac{\sqrt{\pi}}{12}\ \frac{\exp(2\sqrt{aU})}{a^{1/4}U^{5/4}}\ \frac{1}{\sqrt{2\pi}\sigma} \tag{8}$$

$$f(U,J) = \frac{2J+1}{2\sigma^2}\ \exp\left[\frac{-\left(J+\frac{1}{2}\right)^2}{2\sigma^2}\right] \tag{9}$$

with

$$a = \tilde{a}\left[1 + \delta W \frac{1-\exp(-\gamma U)}{U}\right] \tag{10}$$

(Iljinov *et al.* 1992). Microscopic ground state energies from (Möller *et al.* 1995) are adopted as the shell corrections δW, as suggested in (Rauscher *et al.* 1997). The parameter γ describes how quickly the energy dependence of the level density parameter vanishes (i.e. how quickly a approaches its asymptotic value $\tilde{a}$ with increasing energy), and is generally in the range of $0.04 - 0.08$.

The spin cutoff parameter σ^2 in Equation 8 has been defined in a few different ways. The parameterization used by both WHFZ and RT is

$$\sigma^2 = 0.01496\ A^{5/3}\sqrt{\frac{U}{a}} \tag{11}$$

though it may also be given by

$$\sigma^2 = 0.0888\sqrt{aU}A^{2/3} \tag{12}$$

as in the GNASH code (Chadwick 1998). In developing local systematics for the level density parameters, we consider both prescriptions.

The backshift Δ, which defines a false ground state for nuclei containing paired nucleons, has also been given multiple parameterizations. WFHZ use

$$\Delta = P_n + P_p - \frac{\eta}{A} \tag{13}$$

with $\eta = 80$ and pairing energies P_n and P_p from (Gilbert & Cameron 1965). Similar values can be acquired by considering the differences in binding energies between neighboring nuclei, as is done in (Rauscher *et al.* 1997). Using this method, one has

$$\begin{aligned}
\Delta_p &= B_{Z,N} - \frac{1}{2}\left[B_{Z-1,N} + B_{Z+1,N}\right] \\
\Delta_n &= B_{Z,N} - \frac{1}{2}\left[B_{Z,N-1} + B_{Z,N+1}\right] \\
\Delta &= \frac{1}{2}(\Delta_p + \Delta_n)
\end{aligned} \tag{14}$$

where $B_{Z,N}$ is the binding energy of the nucleus (Z,N). In developing our level density systematics, we consider the second of these methods, as well as $\Delta = \Delta'_p + \Delta'_n$ where the Δ' are zero for paired nucleons.

Once prescriptions for σ^2, Δ, and δW have been chosen, the only undetermined level density parameters are γ and $\tilde{a}$. For a given value of γ, $\tilde{a}$ can be fit in such a way that it reproduces measured s-wave resonance spacings at the neutron binding energy (D_0), via the relation

$$D_0 = \frac{2}{\rho(B_n - \Delta, \frac{1}{2})} \tag{15}$$

for target nuclei with a ground state spin of zero and

$$D_0 = \frac{2}{\rho(B_n - \Delta, s+\frac{1}{2}) + \rho(B_n - \Delta, s-\frac{1}{2})} \tag{16}$$

for other nuclei with ground state spin s. For nuclei without measured D_0, systematic values of $\tilde{a}$ must be adopted.

To simultaneously determine the best values to use for γ and $\tilde{a}$, we assume a functional form of

$$\tilde{a} = \alpha A + \beta A^{2/3} \tag{17}$$

as in (Rauscher *et al.* 1997) and make a χ^2 fit to known D_0 to obtain the parameters α, β, and γ. We only include the measured D_0 in our local region of interest ($20 \leq Z \leq 29$). RT employ this method globally, using all available D_0 measurements. WFHZ do not use an energy dependent

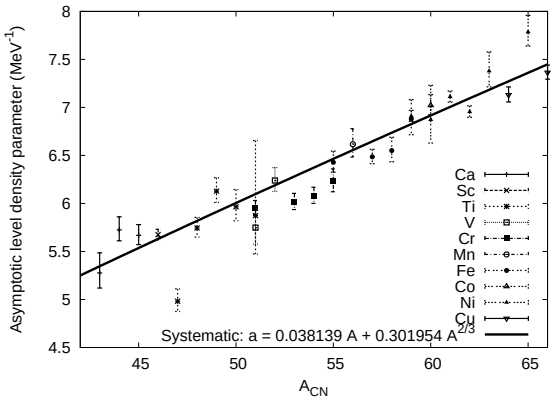

Fig. 1.— χ^2 fit to derived level density parameters.

level density parameter, but include the Gilbert and Cameron shell corrections in thier level density parameter.

In making our least squares fit for the level density parameters, we have considered each of the parameterizations for the spin cutoff parameter and backshift mentioned above. We also consider a case where γ is fixed at the value of 0.04884 obtained in the global fit of (Rauscher *et al.* 1997). The smallest χ^2 is obtained using Equation 11 for the spin cutoff parameter and Equation 14 for the backshift. This results in the set of parameters $\gamma = 0.070036$, $\alpha = 0.038139$, and $\beta = 0.301954$. This systematic is shown in comparison to "experimental" $\tilde{a}$ (determined from measured D_0 using our preferred prescriptions for σ and Δ and $\gamma = 0.070036$) in Figure 1.

This local systematic is superior with respect to the replication of measured resonance spacings, as may be seen in Table 1. In this table, the values listed under RT and WFHZ are calculated using their respective global systematics for level density parameters. The values listed under KHD are calculated using our local systematic. Asterisks following a value indicate that the value is within the errors of the measurement. Values are listed by compound nucleus (target plus neutron). Quantitatively, the performance of a systematic is expressed in terms of the factor of merit g, given by

$$g^2 = \frac{1}{N}\sum_{i=1}^{N}\left(\frac{y_i - x_i}{\sigma_i}\right)^2 \qquad (18)$$

where the y_i are the measured data with errors σ_i and the x_i are the calculated values. The sum extends over all compound nuclei listed in the table. A small factor of merit indicates that a given systematic did well in replicating the experimental values.

Even though we have predicted systematic values for $\tilde{a}$ for these nuclei, in our cross section calculations we use the "experimental" values shown in Figure 1. Systematic values are only used when in cases where there is not a measured D_0.

The state density (Eqn. 8) diverges and the spin cutoff parameter becomes imaginary at $E = \Delta$. At these low energies, the nuclear level density is better described by a constant temperature formula (Gilbert & Cameron 1965):

$$\rho(E) = \frac{1}{T}\exp\left[\frac{E - E_0}{T}\right]\frac{1}{\sqrt{2\pi\sigma^2}}. \qquad (19)$$

The Fermi gas and constant temperature state densities are required to match tangentially at an energy E_x which lies between Δ and B_n. The spin cutoff parameter below E_x has been treated several different ways (Reffo 1978; Chadwick 1998). We hold it constant at its value at E_x. The tangential matching requirement fixes the values of E_0 and T for a given E_x, and E_x may be fit in such a way that the integrated level density matches the cumulative number of discrete levels. Each nucleus is fit individually, as opposed to using an systematic matching energy such as that suggested in (Gilbert & Cameron 1965). RT similarly employ a constant temperature state density at low excitation energies. WFHZ deal with the divergence in the Fermi gas state density by assuming that the state density remains constant between $E = 0.5$ MeV and $E = 4/a + \Delta$, and falls to zero below 0.5 MeV. Such an assumption has no effect when the discrete level scheme is complete up to $E = 4/a + \Delta$.

2.3. Particle Transmission Coefficients

For the calculation of neutron and proton transmission coefficients, we utilize the optical model of (Koning & Delaroche 2003) (hereafter KD03).

Table 1: S-wave resonance spacings from various level density presciptions, in keV, compared to measured values from the Reference Input Parameter Library. Asterisks indicate that a calculated value is within the errors of the measurement. The last line of the table is a figure of merit described in the text.

^{A}Z	RIPL	WFHZ		RT		KHD	
^{43}Ca	20.0 ± 5.0	52.6		39.4		18.2	*
^{44}Ca	1.80 ± 0.30	4.98		5.74		2.65	
^{45}Ca	24.1 ± 3.2	65.4		51.6		28.5	
^{46}Sc	1.30 ± 0.10	2.93		3.15		1.38	*
^{47}Ti	25.0 ± 4.4	29.6		12.6		8.50	
^{48}Ti	1.75 ± 0.25	3.48		2.72		1.58	*
^{49}Ti	18.3 ± 2.9	46.5		43.9		24.0	
^{50}Ti	4.00 ± 0.80	4.93		5.35		3.80	*
^{51}Ti	125 ± 70	127	*	125	*	98.1	*
^{51}V	2.30 ± 0.60	2.99		1.59		1.45	
^{52}V	4.10 ± 0.60	5.51		5.90		4.34	*
^{51}Cr	13.3 ± 1.3	25.7		19.3		11.0	
^{53}Cr	43.4 ± 4.4	50.3		37.1		31.7	
^{54}Cr	7.80 ± 0.80	7.07	*	7.76	*	5.48	
^{55}Cr	62.0 ± 8.0	75.5		58.2	*	48.2	
^{56}Mn	2.30 ± 0.40	3.73		2.42	*	2.47	*
^{55}Fe	18.0 ± 2.4	37.8		18.1	*	17.2	*
^{57}Fe	25.4 ± 2.2	47.8		21.4		21.1	
^{58}Fe	6.50 ± 1.00	7.66		5.91	*	5.19	
^{59}Fe	25.4 ± 4.9	51.2		24.4	*	26.9	*
^{60}Co	1.25 ± 0.15	2.09		1.43		1.41	
^{59}Ni	13.4 ± 0.9	31.0		13.7	*	14.7	
^{60}Ni	2.00 ± 0.70	2.39	*	2.15	*	1.90	*
^{61}Ni	13.8 ± 0.9	29.8		17.3		15.5	
^{62}Ni	2.10 ± 0.15	2.04	*	1.71		1.78	
^{63}Ni	16.0 ± 3.0	29.0		21.4		19.6	
^{65}Ni	19.6 ± 3.0	32.0		35.8		29.6	
^{64}Cu	0.95 ± 0.09	1.23		0.60		0.80	
g	–	8.07		5.41		1.76	

Although they have tuned their parameters to fit data for many different nuclear species, we have used the global nucleon-nucleus potential, as it gives a satisfactory fit to measured total neutron cross section data in the region of interest to us. Additionally, this potential provides reasonable values for s- and p-wave strength functions and potential scattering radii in this mass region. Transmission coefficients were generated from the optical potential using the ECIS-95 code (Raynal 1996). Although designed for coupled channel calculations, we use the code in a spherical mode.

Previous modeling efforts have relied on other optical potentials. RT use the potential of (Jeukenne *et al.* 1977), hereafter JLM77. WFHZ use an equivalent square well potential (Michaud & Fowler 1970), primarily because the transmission coefficients can be written in closed form, saving considerable computation time. The Woods-Saxon potentials of KD03 and JLM77 provide a more accurate representation of the nuclear potential, and we do not consider the square well potential further in our analysis.

We present in Figure 2 the total neutron cross section for ^{56,57,58}Fe targets as calculated using the KD03 and JLM77 optical potentials. The calculations are plotted against measured data from (EXFOR). Error bars have been omitted for clarity. The cross sections derived from the KD03 model compare favorably to the experimental data, but not significantly better or worse than those of JLM77. Comparisons using stable Cr, Mn, Co, and Ni targets yield similar results.

In Figure 3 we present the ratios of model derived s- and p-wave strength functions and potential scattering radii to measured values. The dotted lines mark a factor of two from unity. The KD03 model is superior to JLM77 in the replication of these values over the entire mass range presented, but both models do reasonably well around $A = 60$.

We also include alpha particle and deuteron exit channels in our modeling effort, using the optical potentials of (McFadden & Satchler 1966) and (Perey & Perey 1963), respectively. However, The transmission coefficients for charged particles are supressed by a Coulomb barrier at low energies, and will not significantly affect modeled neutron capture cross sections.

2.4. Photon Transmission Coefficients

Our photon transmission coefficients depend only on the multi-pole type (XL) and the transition energy (ϵ). They are related to the gamma ray strength function $f^{\gamma}_{XL}(\epsilon)$ by

$$T^{\gamma}_{XL}(\epsilon) = 2\pi\epsilon^{2L+1} f^{\gamma}_{XL}(\epsilon). \qquad (20)$$

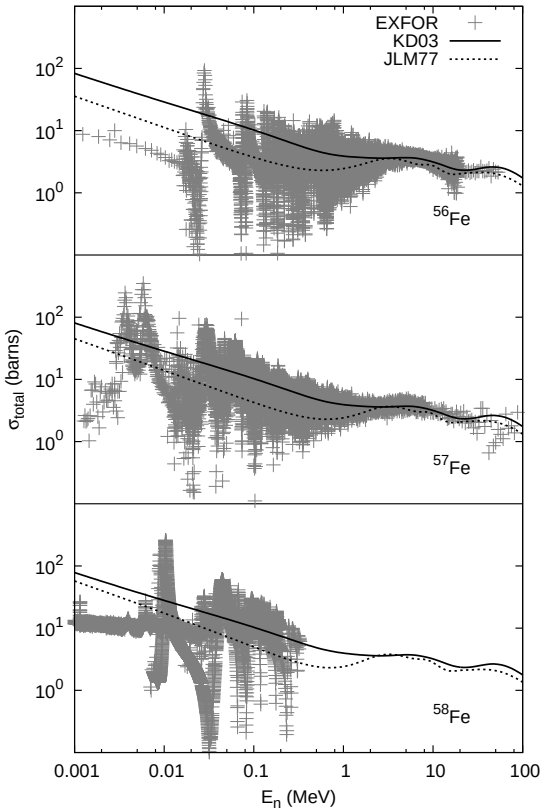

Fig. 2.— Total neutron Cross Sections as calculated from the KD03 and JLM77 optical potentials, compared to measured cross sections.

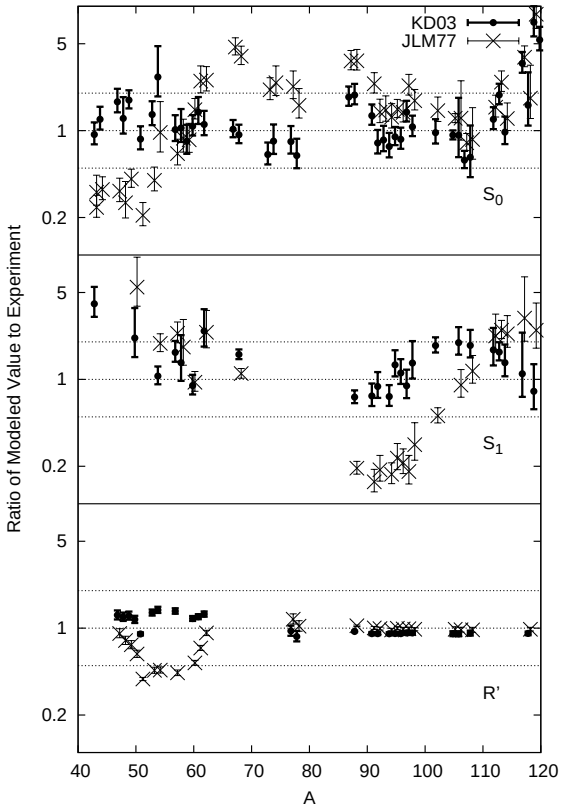

Fig. 3.— Ratios of s- and p-wave strength functions and potential scattering radii derived from KD03 and JLM77 optical potentials to measured values.

The energy dependence of the E1 strength function is determined using the Enhanced Generalized Lorentzian model (EGLO)

$$f^{\gamma}_{E1}(\epsilon) = \mathcal{N}_{E1}\frac{4}{3\pi}\frac{e^2}{\hbar c}\frac{1}{M_p c^2}\times \sum_{GDR}\left[\frac{\epsilon\Gamma_{GDR}(\epsilon,T_f)}{(\epsilon^2-E^2_{GDR})^2+(\Gamma_{GDR}(\epsilon,T_f)\epsilon)^2}+ 0.7\frac{\Gamma_{GDR}(0,T_f)}{\epsilon^3}\right] \quad (21)$$

where M_p is the proton mass. The energy dependent width $\Gamma_{GDR}(\epsilon,T_f)$ is given by

$$\Gamma_{GDR}(\epsilon,T_f) = \left[\kappa+(1-\kappa)\frac{\epsilon-\epsilon}{E_{GDR}-\epsilon}\right]\times \frac{\Gamma_{GDR}}{E^2_{GDR}}\left[\epsilon^2+(2\pi T_f)^2\right] \quad (22)$$

with $\epsilon = 4.5$ MeV. For nuclei with $A < 148$, the factor κ is unity. For heavier nuclei, $\kappa = 1+0.009(A-148)^2\exp[-0.18(A-148)]$. The T_f that appears in Equations 21 and 22 is the temperature of the final state, determined from the level density parameters. For a backshifted transition energy $U = S_n - \epsilon - \Delta$, one determines the energy dependent level density parameter (Eqn. 10). Provided U is positive, the temperature is given by

$$T_f = \frac{a}{2}\left[1+\sqrt{1+4aU}\right]. \quad (23)$$

Otherwise, $T_f = 1/a$. The $\mathcal{N}_{E1}$ appearing in Equation 21 is an overall normalization constant that will be described in the next section. We include two GDR resonances in the description of the E1 strength function. In many cases, the energies, widths, and peak cross sections of the

resonances have been experimentally determined (RIPL). We use these measured values where available. Where such data is not available we have developed the following set of systematics by making a χ^2 fit to measured parameters in the region of interest

$$\begin{aligned} E_{GDR1} &= -0.1079\ A\ +\ 23.22 \\ \Gamma_{GDR1} &= -0.0118\ A\ +\ 5.73 \\ \sigma_{GDR1} &= 0.1050\ A\ +\ 57.25 \\ E_{GDR2} &= -0.1695\ A\ +\ 29.47 \\ \Gamma_{GDR2} &= -0.0134\ A\ +\ 7.39 \\ \sigma_{GDR2} &= 2.125\ A\ -\ 75.27. \end{aligned} \quad (24)$$

The peak cross section (σ_{GDR}) provides an overall multiplicative factor to the strength function and can be absorbed into the overall normalization.

For the M1 strength function, we adopt a Simple Lorentzian (SLO) model

$$f^{\gamma}_{M1}(\epsilon) = \mathcal{N}_{M1}\frac{4}{3\pi}\frac{e^2}{\hbar c}\frac{1}{M_p c^2} \times \sum_{GDR}\frac{\epsilon\Gamma_{GDR}}{(\epsilon^2 - E^2_{GDR})^2 + (\Gamma_{GDR}\epsilon)^2} \quad (25)$$

with the global set of GDR parameters given in (RIPL):

$$\begin{aligned} E_{GDR} &= \frac{41}{A^{1/3}} \\ \Gamma_{GDR} &= 4. \end{aligned} \quad (26)$$

The overall normalization for the M1 strength function ($\mathcal{N}_{M1}$) is determined such that

$$\frac{f_{E1}(S_n)}{f_{M1}(S_n)} = 0.0588 \cdot A^{0.878} \quad (27)$$

where S_n is the neutron separation energy.

We also include E2, M2, E3, and M3 transitions with Blatt-Weisskopf strength functions (Blatt & Weisskopf 1952), normalized to

$$\begin{aligned} f^{\gamma}_{E2}(S_n) &= 7.2\times10^{-7}A_C^{2/3}f^{\gamma}_{E1}(S_n) \\ f^{\gamma}_{M2}(S_n) &= 2.2\times10^{-7}f^{\gamma}_{E1}(S_n) \\ f^{\gamma}_{E3}(S_n) &= 3.4\times10^{-13}A_C^{4/3}f^{\gamma}_{E1}(S_n) \\ f^{\gamma}_{M3}(S_n) &= 1.1\times10^{-13}A_C^{2/3}f^{\gamma}_{E1}(S_n). \end{aligned} \quad (28)$$

Previous modeling efforts (RT, WFHZ) utilize an SLO representation for the E1 strength function and a Blatt-Weisskopf M1 strength function. It has been suggested (RIPL) that the SLO overestimates the E1 strength function at low photon energies. WFHZ use a set of GDR parameters that depend only on the mass number of the compound nucleus (with empirical provisions for closed shell and near-closed shell nuclei) , while RT use an energy dependent GDR width that accounts for nuclear deformation. Both use a single resonance. We will show in section 5 that the ^{59}Fe(n,γ)^{60}Fe and ^{60}Fe(n,γ)^{61}Fe cross sections, and hence the reaction rates, are somewhat sensitive to the representation of the strength functions (i.e. EGLO v. SLO), but almost completely insensitive to the GDR parameters.

3. Normalization of the E1 Strength Function

We now consider the overall normalization of the E1 strength function. As will be seen in section 5, modeled neutron capture reactions are more sensitive to this quantity that any other input parameter, and hence it is of primary importance.

As mentioned, WFHZ and RT have adopted an SLO representaion for the E1 strength function (see Eqn. 25). The E1 normalization is determined by an empirical fit to Maxwellian-averaged cross sections (MACS) for neutron capture. The MACS is related to the laboratory cross section in a manner similar to the reaction rate:

$$\begin{aligned} \frac{\langle\sigma v\rangle}{v_T} &= \frac{\int_0^\infty \sigma_{n\gamma} v\Phi(v)dv}{v_T} \\ &= \frac{2}{\sqrt{\pi}(k_BT)^2}\int_0^\infty \sigma_{n\gamma}(E)W(E,k_BT)dE \end{aligned} \quad (29)$$

where $W(E,k_BT) = E\exp(-E/k_BT)$ and E is the center of mass energy. Many neutron capture MACS have been measured, and a current tabulation of recommended values at $k_BT = 30$ keV is provided by (Bao *et al.* 2000). The process of normalizing to MACS involves calculating the cross section assuming $\mathcal{N}_{E1} = 1$, finding the ratios of the calculated MACS at 30 keV to the measured values, and looking for systematic behavior. Since the photon transmission coefficients are very small in comparison to the neutron transmission coefficients at low excitation energies, and since charged particle transmission coefficients are suppressed by the Coulomb barrier, the Hauser-Feshbach denominator (Eqn. 3) will be dominated

by the neutron channels. Thus the neutron transmission coefficient in the numerator of Equation 2 will roughly cancel with the denominator, making the cross section approximately proportional to any multiplicative constant in the photon transmission coefficient. This being the case, one may find the ratio of the measured 30 keV MACS to the value calculated using an overall E1 normalization of unity and substitute that value for $\mathcal{N}_{E1}$. The resulting neutron capture cross section will then replicate the measured 30 keV MACS to within a small error. WFHZ and RT considered the global systematic behavior of the measured to calculated MACS ratio, and found the following empirical normalizations:

$$\begin{aligned} \text{WFHZ} \quad &: \quad \mathcal{N}_{E1} = \kappa_E \frac{NZ}{A} \\ \text{RT} \quad &: \quad \mathcal{N}_{E1} = (1+\chi)\frac{NZ}{A} \end{aligned} \tag{30}$$

where $\kappa_E = 0.25$ and $\chi = 0.2$. Differences in the overall normalizations arise from differences in the GDR parameters, the energy dependent GDR width used by RT, and the greater abundance of measured MACS data available to RT.

Another method for normalizing the E1 strength function involves fitting $\mathcal{N}_{E1}$ to average total s-wave radiation widths ($\langle\Gamma_\gamma\rangle_0$). This quantity, which can be measured in neutron resonance experiments, may be calculated from the level densities and photon transmission coefficients as

$$\begin{aligned} \langle\Gamma_\gamma\rangle_0 \quad = \quad & \frac{J_t+1}{2J_t+1}\left\langle\Gamma_\gamma\left(B_n, J_t+\frac{1}{2}, \Pi_t\right)\right\rangle + \\ & \frac{J_t}{2J_t+1}\left\langle\Gamma_\gamma\left(B_n, J_t-\frac{1}{2}, \Pi_t\right)\right\rangle \end{aligned} \tag{31}$$

Here, B_n is the neutron binding energy of the compound nucleus in question, and J_t is the ground state spin of the nucleus formed by the emission of a single nuetron from the compound nucleus. The total widths of the two resonances are given by

$$\begin{aligned} \langle\Gamma\gamma(E,J,\Pi)\rangle \quad = \quad & \frac{1}{2\pi\rho(E,J,\Pi)i} \times \\ & \sum_{XL}\sum_{J_f,\Pi_f}\left[\sum_{\nu=1}^{\omega} T_\gamma^{XL}(E-E_\nu, J_\nu, \Pi_\nu) + \right. \\ & \left. \int_0^{E-E_\omega} d\epsilon\; T_\gamma^{XL}(\epsilon, J_f, \Pi_f)\rho(E-\epsilon, J_f, \Pi_f)\right]. \end{aligned} \tag{32}$$

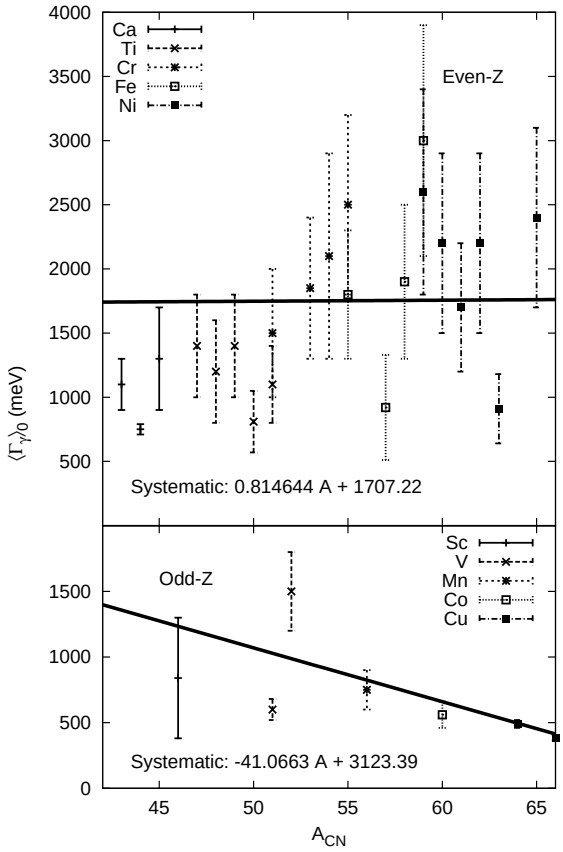

Fig. 4.— Systematics for average total s-wave radiation width.

Here, the sum extends over all possible final state spins (J_f) and parities (Π_f). To normalize the E1 strength function using $\langle\Gamma_\gamma\rangle_0$, one first assumes $\mathcal{N}_{E1}$ is equal to unity and calculates the average radiation width. Since $\langle\Gamma_\gamma\rangle_0$ is proporitonal to $\mathcal{N}_{E1}$, the proper normalization needed to replicate the measured value will be

$$\mathcal{N}_{E1} = \frac{\langle\Gamma_\gamma\rangle_0^{\text{meas.}}}{\langle\Gamma_\gamma\rangle_0^{\mathcal{N}_{E1}=1}}. \tag{33}$$

Although $\langle\Gamma_\gamma\rangle_0$ has only been measured for a few select nuclei, the behavior of the widths generally varies smoothly as a function of mass so that systematics may be developed. This method of normalizing the E1 strength function has proven effective in previous modeling efforts (Hoffman *et al.* 2004).

Our local systematics for $\langle\Gamma_\gamma\rangle_0$ may be seen in Figure 4. The variation of $\langle\Gamma_\gamma\rangle_0$ in the our

Table 2: Comparison of experimental and modeled 30 keV Maxwellian-averaged neutron capture cross sections, in mb. Asterisks following a calculated value indicate that it is within the errors of the measurement.

Target	Recommended	WFHZ		RT		KHD		KHD2	
^{50}Cr	49 ± 13	34		44.8	*	58.2	*	58.7	*
^{51}Cr	87 ± 16	63		86.0	*	137.9		131.1	
^{52}Cr	8.8 ± 2.3	12		16.7		23.1		12.2	
^{53}Cr	58 ± 10	24		26.0		35.7		34.5	*
^{54}Cr	6.7 ± 1.6	7.2	*	9.4		25.1		12.0	
^{55}Mn	39.6 ± 3.0	28		35.5		49.9		46.3	
^{54}Fe	27.6 ± 1.8	28	*	46.5		52.4		34.7	
^{55}Fe	75 ± 12	46		83.9	*	88.3		85.9	*
^{56}Fe	11.7 ± 0.5	19		26.2		23.3		11.0	*
^{57}Fe	40 ± 4	21		30.3		27.1		33.9	
^{58}Fe	12.1 ± 1.3	9.5		12.9	*	61.8		26.1	
^{59}Co	38 ± 4	36	*	51.3		59.8		30.1	
^{58}Ni	41 ± 2	29		50.5		78.6		54.3	
^{59}Ni	87 ± 14	72		92.4	*	130.9		83.8	*
^{60}Ni	30 ± 3	20		33.2		55.4		30.6	*
^{61}Ni	82 ± 8	37		77.8	*	104.1		57.9	
^{62}Ni	12.5 ± 4.0	12	*	19.2		37.1		13.3	*
^{63}Ni	31 ± 6	24		36.5	*	70.9		44.5	
^{64}Ni	8.7 ± 0.9	6.1		10.1		63.7		15.2	
g	–	4.399		7.349		18.762		3.823	

range of interest is not as smooth as in higher mass regions, but does exhibit some general systematic behavior. We note that the measured $\langle\Gamma_\gamma\rangle_0$ in this region are also significantly larger than those for nuclei of larger mass. Our systematic was found by making a χ^2 linear fit to the measured data, with separate sytematics being developed for even- and odd-Z nuclei. Whenever they are available, we normalize to measured $\langle\Gamma_\gamma\rangle_0$ when calculating cross sections.

In Tables 2 and 3 we list the MACS and $\langle\Gamma_\gamma\rangle_0$ computed from the input prescriptions of WFHZ, RT, and the present work. We note that the MACS for WFHZ and RT were taken directly from the CRSEC and NONSMOKER codes utilized by these groups. The tables also include the recommended MACS from (Bao *et al.* 2000) and measured $\langle\Gamma_\gamma\rangle_0$ from (RIPL). The results in the column labeled KHD in Table 3 are normalized to systematic $\langle\Gamma_\gamma\rangle_0$ only, since normalization to measured values would result in exact replication in every case. The respective results in Table 2 involve a normalization to measured $\langle\Gamma_\gamma\rangle_0$. The last column in each table (labeled KHD2) lists results that involve a secondary normalization, which will be discussed shortly. Also included is a factor of merit g (see Eqn. 18).

What we note at this point is that our prescription for normalizing the E1 strength function, when combined with our other statistical model inputs, is superior in replicating measured $\langle\Gamma_\gamma\rangle_0$ but tends to overestimate the MACS. WFHZ and RT tend to underestimate $\langle\Gamma_\gamma\rangle_0$ but do much better on the MACS. This result is not terribly surprising, since WFHZ and RT normalize the E1 strength function to 30 keV MACS, while we have normalized to the measured $\langle\Gamma_\gamma\rangle_0$. We note that a few of the measrued $\langle\Gamma_\gamma\rangle_0$, namely those for ^{59}Fe, ^{59}Ni, and ^{65}Ni, are particularly high compared to other nuclei in the near vicinity. Correspondingly, our MACS for ^{58}Fe(n,γ)^{59}Fe, ^{58}Ni(n,γ)^{59}Ni, and ^{64}Ni(n,γ)^{65}Ni are very high.

The (n,γ) rates used in nucleosynthesis studies (Woosley & Weaver 1995; Rauscher *et al.* 2002) are normalized to agree with the recommended MACS at 30 keV (for RT renormalizations, see (Bao *et al.* 2000)). For a comparison of 30 keV

Table 3: Modeled average totat s-wave radiation widths (in meV) compared to measured data. Asterisks following a calculated value indicate that it is within the error of the measurement.

Compound Nucleus	Measured	WFHZ		RT		KHD		KHD2	
^{51}Cr	1500±500	754.69		1202.40	*	1748.77	*	1468.12	*
^{53}Cr	1850±550	579.41		738.69		1750.40	*	803.63	
^{54}Cr	2100±800	418.80		1348.90	*	1751.21	*	3274.05	
^{55}Cr	2500±700	458.37		733.34		1752.03		930.33	
^{56}Mn	750±150	381.91		722.51	*	823.68	*	676.33	*
^{55}Fe	1800±500	1060.90		1170.20		1752.03	*	973.08	
^{57}Fe	920±410	786.08	*	1088.30	*	1753.65		340.74	
^{58}Fe	1900±600	758.93		1300.10	*	1754.47	*	2362.64	*
^{59}Fe	3000±900	429.09		542.33		1755.28		929.81	
^{60}Co	560±100	358.42		510.03	*	659.41		251.62	
^{59}Ni	2600±800	891.70		944.93		1755.28		1417.83	
^{60}Ni	2200±700	516.14		971.08		1756.10	*	1266.20	
^{61}Ni	1700±500	477.52		1050.60		1756.91	*	717.84	
^{62}Ni	2200±700	428.43		917.04		1757.73	*	1021.72	
^{63}Ni	910±270	314.44		629.14		1758.54		243.15	
^{65}Ni	2400±700	217.29		430.80		1760.17	*	360.42	
g	–	2.263		1.650		1.162		1.877	

cross sections from WFHZ and RT over the mass range from $20 \leq A \leq 85$, see figures 10 and 11 in (Hoffman *et al.* 1999).

These results seem to indicate that the measured MACS and $\langle\Gamma_\gamma\rangle_0$ cannot be simultaneously replicated. We then must ask ourselves which quantity we are most interested in reproducing. Ultimately our goal is to provide the best possible rates for ^{59}Fe(n,γ)^{60}Fe and ^{60}Fe(n,γ)^{61}Fe, which are directly related to the cross sections, i.e. it is the cross sections that we need to do well on. To this end, we should normalize to the MACS. However, we do not wish to completely abandon the ties to measured radiation widths, so we proceed by making a secondary normalization.

Global systematics for $\langle\Gamma_\gamma\rangle_0$ seem to indicate that the quantity is a function of both mass and s-wave resonance spacing (Gardner 1975). Using this as a guide, we consider the ratio of the measured MACS to our calculated MACS as a function of A and D_0, shown in figure 5. The ratios appear to slowly decrease in a linear fashion with increasing mass. The behavior as a function of D_0 is quite different. A nearly Lorentzian behavior is noted. So our chosen fitting function for the measured to calculated MACS ratio is of the form

$$\xi(A, D_0) = (c_1 A + c_2)\left[\frac{c_3 c_4^2 D_0}{(D_0^2 - c_5^2)^2 + (c_4 c_5)^2} + c_6\right]. \tag{34}$$

A weighted fit to the calculated ratios yields the following values for the fitting constants:

$$\begin{aligned} c_1 &= -0.028281 \\ c_2 &= 1.958639 \\ c_3 &= 1.747113 \\ c_4 &= 38.080159 \\ c_5 &= -1.648677 \\ c_6 &= 0.913862. \end{aligned} \tag{35}$$

This factor is then applied as a secondary normalization to the E1 strength function, so that we now have

$$\mathcal{N}_{E1}(A, D_0) = \xi(A, D_0)\frac{\langle\Gamma_\gamma\rangle_0^{\text{meas/sys}}}{\langle\Gamma_\gamma\rangle_0^{\mathcal{N}_{E1}=1}}. \tag{36}$$

Measured values for $\langle\Gamma_\gamma\rangle_0$ are used when they are available, otherwise the systematics of Figure 4 are employed.

As expected, the application of this secondary normalization greatly improves our ability to replicate measured 30 keV MACS, while unraveling our

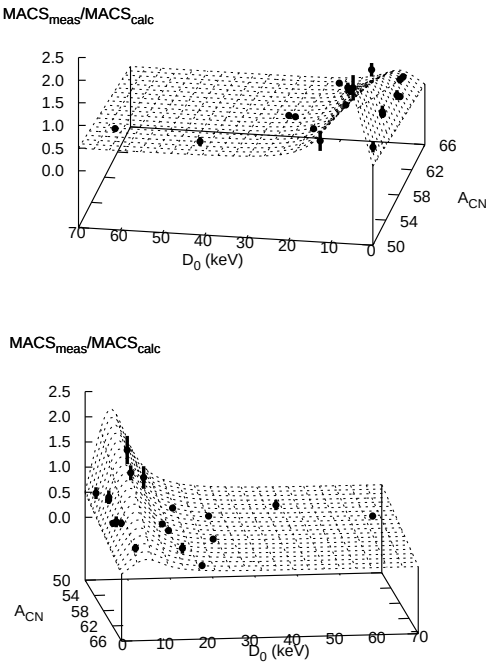

Fig. 5.— Systematic for secondary normalization of the E1 strength function. The surface is viewed from two separate angles. Error bars reflect the errors in measured Maxwellian averaged cross sections.

favorable comparison to measured $\langle\Gamma_\gamma\rangle_0$. In Table 2, we see that our calculations with this secondary normalization (column labeled KHD2) are superior at replicating the measured values, as indicated by the factor of merit. With regards to the measured $\langle\Gamma_\gamma\rangle_0$, the RT perform better than our calculation with the secondary normalization, though not by much. Given that our goal is to replicate cross sections, we feel that our second calculations are favorable over the others.

4. Results and Comparisons

Table 2 provides a first indication of the success of our modeling effort. With the exception of ^{58}Fe(n,γ)^{59}Fe, our modeled MACS are within a factor of two of the measured values, and typically within 30%.

As an additional check on the quality of our calculations, we compare our results (and those of WFHZ and RT) to measured cross section data in Figure 6. The measured data is a compilation of data sets available on (EXFOR). No effort has been made to evaluate the quality of the various data sets, and all have been included. Error bars have been omitted for clarity. Our calculated cross section is represented by a thick solid line. The results from WFHZ, as obtained from the CRSEC code, are represented by the dashed lines. The results from the NONSMOKER code implemented by RT are represented by the dotted lines.

The majority of measured neutron capture cross section data lies in the resonance region, and hence is not of much use in evaluating statistical model calculations. For a few of the targets considered (specifically ^{55}Mn, ^{56,58}Fe, ^{59}Co, and ^{60,64}Ni) a limited amount of data is available above the resonances, though at this point the cross sections are generally only on the order of 10 mb. We are primarily interested in replicating the cross section at 30 keV of incident energy, and the comparison to measured Maxwellian averaged cross sections (Table 2) provides a more suitable means of evaluating the performance of the various calculations.

In Figure 7 we present our modeled reaction rates for ^{59}Fe(n,γ)^{60}Fe and ^{60}Fe(n,γ)^{61}Fe. We also provide for comparison the reaction rates of WFHZ and RT. The modern rates are larger than WFHZ for both targets, with our rates being the highest in both cases.

We have modeled other additonal neutron induced cross sections in this region of interest. For these reactions, our modeled cross sections compare favorably to measured cross section data.

5. Sensitivity of Reaction Rates to Variations in Input Parameters

We now consider the approximate uncertainties in our reaction rates with respect to the various input quantities. These uncertainties fall into one of two classifications: those associated with uncertainties in our local systematics, and those associated with the choice of prescriptions for the various input parameters. In this section we vary only one input parameter at a time. Collective un-

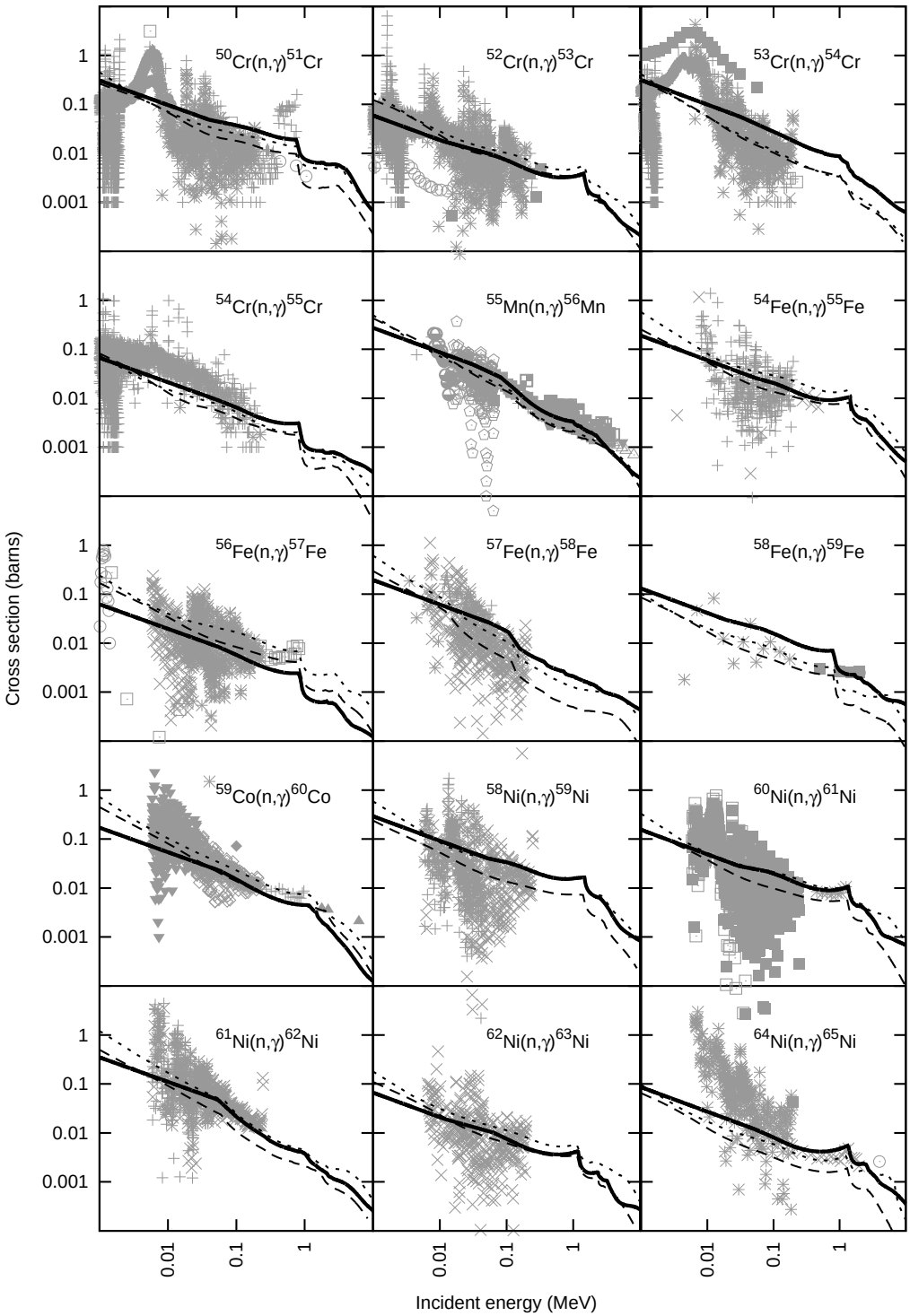

Fig. 6.— Calculated neutron capture cross sections compared to experimental data. The solid line represents our calculation based on local systematics. The dashed and dotted lines represent the calculations of WFHZ and RT, respectively. Data is taken from EXFOR (EXFOR). Error bars have been omitted for clarity.

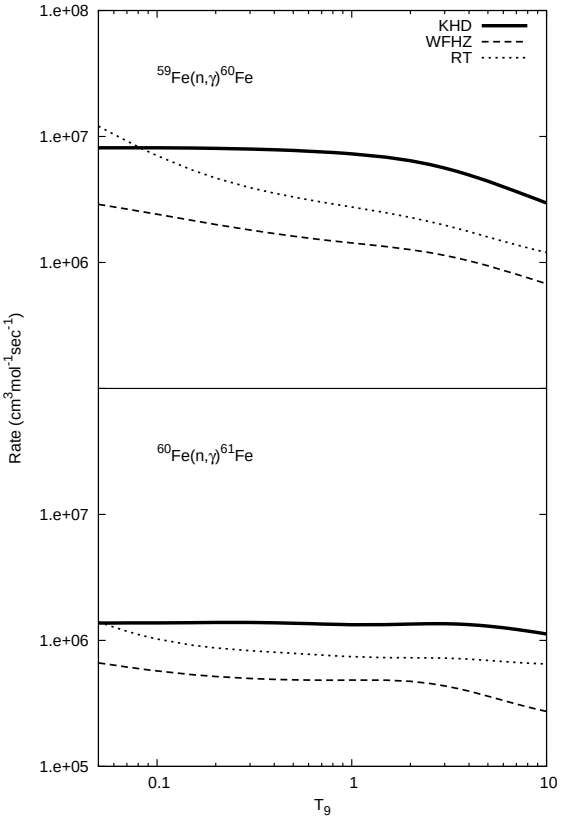

Fig. 7.— Modeled capture reaction rates for ^{59,60}Fe compared to those of WFHZ (dashed lines) and RT (dotted lines).

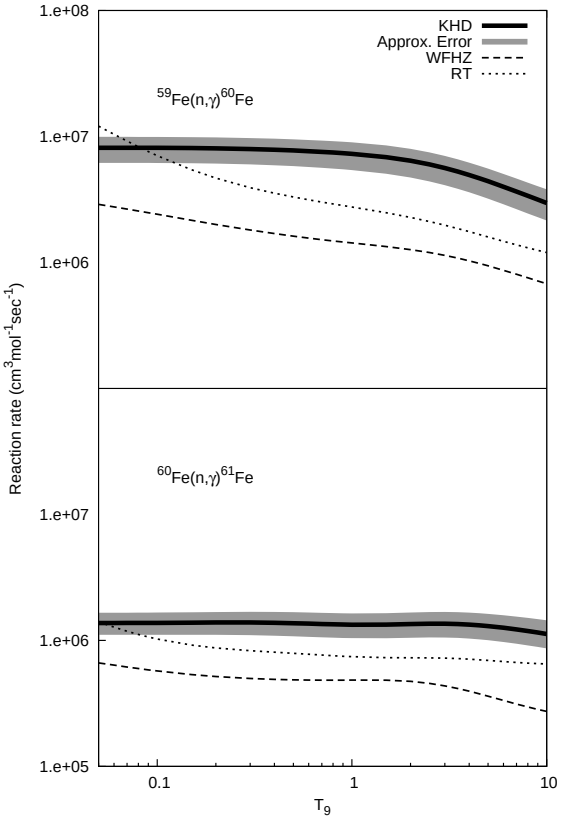

Fig. 8.— Sensitivity of ^{59,60}Fe(n,γ) reaction rates to uncertainties in the level density systematic

certainties including all input parameters will be presented in the conclusions.

5.1. Errors in Systematic Input Parameters

The Hauser-Feshbach input quantities presented in section 2 represent our best estimates given available experimental data. As such, we believe our reaction rates to be as accurate as possible. However, these rates are based on systematics, and any uncertainty associated with the development of these systematics will be reflected in the rates.

5.1.1. Asymptotic Level Density Parameter

The standard deviation of the experimental level density parameters $\tilde{a}$ from our systematic is 0.232 MeV^{-1}, a value somewhat larger than the average errorbar on the experimental values (0.135 MeV^{-1}). We assume that the errors in the level density parameters for ^{60,61}Fe are the same as the standard deviation of the experimental values. We then determine an approximate error in the ^{59,60}Fe neutron capture reaction rates by raising or lowering the $\tilde{a}$ for ^{60,61}Fe by 0.232 MeV^{-1}. The results are shown in Figure 8. The uncertainties in the level density systematic amount to uncertainties in the reaction rates of 22-28% for ^{59}Fe(n,γ)^{60}Fe and 19-28% for ^{60}Fe(n,γ)^{61}Fe.

5.1.2. GDR Parameters

The standard deviations of experimental GDR parameters from our systematic values are 0.482 MeV for the peak energy and 1.721 MeV for the width. Despite the rather large uncertainty in the GDR widths, the resulting uncertainties in the reaction rates for ^{59}Fe(n,γ)^{60}Fe and ^{60}Fe(n,γ)^{61}Fe are negligibly small (less than 1.5% for ^{59}Fe, 0.5%

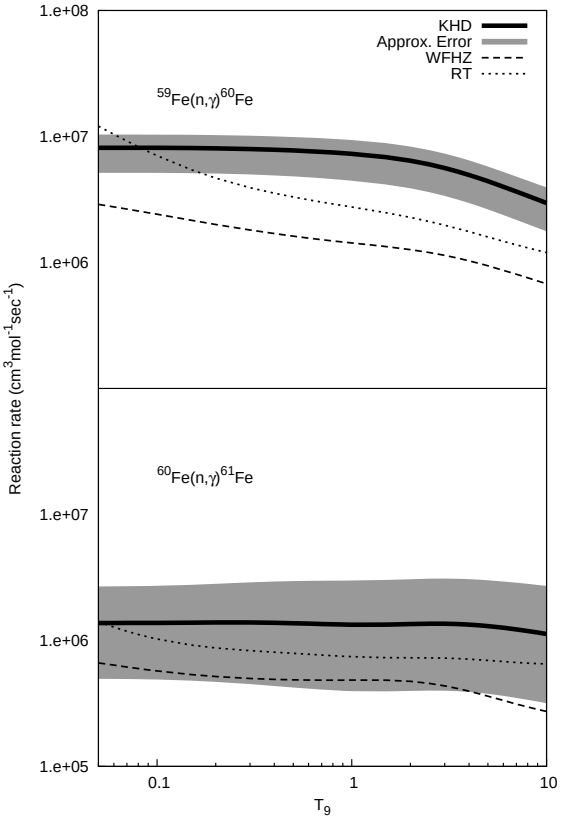

Fig. 9.— Sensitivity to the average s-wave radiation width

for ^{60}Fe).

5.1.3. *Normalization of the γ-ray Transmission Coefficient*

The experimental data for $\langle\Gamma_\gamma\rangle_0$ in our region of interest has an average error of ∼600 meV for all even-Z compund nuclei and ∼160 meV for all odd-Z compound nuclei (see Figure 4). These average errors are similar to the standard deviations of the experimental values from the systematic, which are 630.7 meV and 320.9 meV for even- and odd-Z compound nuclei, respectively. Assuming these values for the uncertainty of the radiation widths of ^{60,61}Fe yields the approximate uncertainties in the reaction rates shown in Figure 9. These uncertainties are in the range of 27-41% for ^{59}Fe(n,γ)^{60}Fe and 63-140% for ^{60}Fe(n,γ)^{61}Fe.

5.2. Variations in Input Parameter Prescriptions

In addition to uncertainties in the reaction rates stemming from the development of our local systematics, we also consider the uncertainties resulting from varying the overall prescription for the Hauser-Feshbach input quantities.

5.2.1. *Level Density Prescription and Discrete Levels*

In the upper panels of Figure 10 we present the sensitivity of the reaction rates where the level density prescription (in conjunction with the proper set of discrete levels) is varied, keeping all other parameter input fixed. The sensitivity is expressed in terms of the percentage change in the reaction rate, defined as

$$\delta\sigma = \frac{\sigma - \sigma_{KHD}}{\sigma_{KHD}} \times 100\% \qquad (37)$$

where σ_{KHD} are our recommended rates from Figure 7. The dotted lines correspond to the rates calculated using the level densities and discrete levels of RT. The dahsed lines represent the rates calculated using the level densities and discrete levels of WFHZ.

These variations in the Fermi gas level density prescriptions change the reaction rates by as much as ∼50%, but generally the change is within 30%. For both reactions, the level densities of RT and WFHZ result in smaller reaction rates.

5.2.2. *Neutron Transmission Coefficients*

The sensitivity to the choice of neutron transmission coefficient is shown in the second row of panels in Figure 10. The uncertainties associated with this input quantity are about half as large as those due to the level density. In this analysis we are keep the level density prescription fixed, using our local systematic. Both of the older optical potentials result in smaller rates, with the difference being more significant for the JLM77 potential (up to ∼30%).

5.2.3. *E1 and M1 Strength Functions*

We employ an EGLO representation of the E1 strength function and an SLO representation for the M1 strength function. The third row of panels

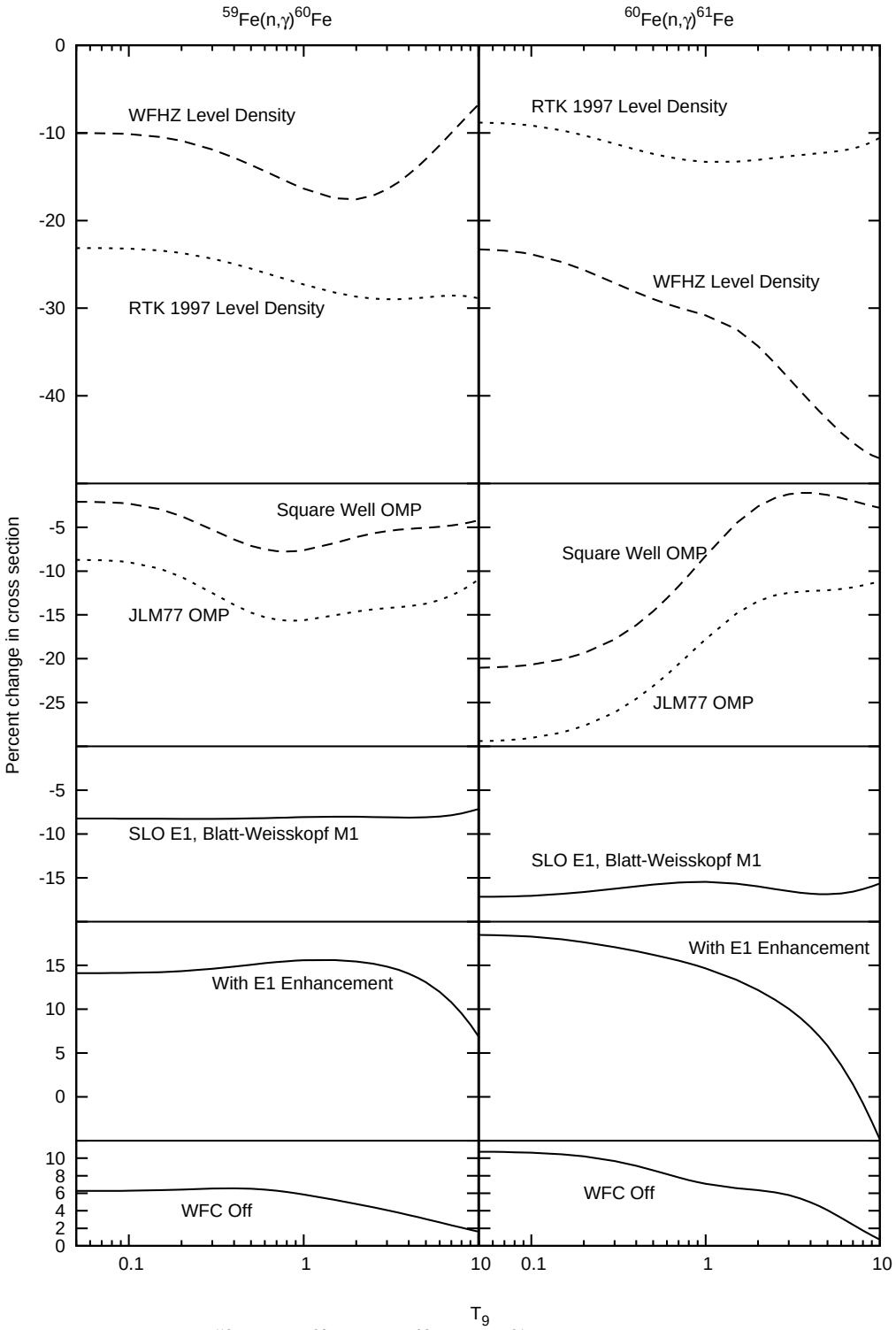

Fig. 10.— Sensitivity of the ^{59}Fe(n,γ)^{60}Fe and ^{60}Fe(n,γ)^{61}Fe rates to choices in statistical model input parameters.

in Figure 10 show the percent change in the reaction rate if one were to use an SLO representation for E1 and Blatt-Weisskopf M1 strength functions. In both cases, the effect is to lower the cross section and reaction rate, by roughly 8% in the case of the ^{59}Fe(n,γ)^{60}Fe and on the order of 15-18% in the case of ^{60}Fe(n,γ)^{61}Fe.

Recently an enhancement of the photon strength function for low energy photons has been measured in iron isotopes (Voinov *et al.* 2004). We present the sensitivity of the reaction rates to this enhancement in the fourth set of panels in Figure 10, assuming that the parameters of the enhancement measured for ^{57}Fe would also apply to heavier iron isotopes. This enhancement increases the reaction rates by roughly 15-20% at low temperatures, with the effect tapering off at higher T_9. Our recommended rates, presented in figure 7, do not include this enhancement.

5.2.4. GDR parameter prescriptions

We have investigated the sensitivity of the reaction rates to the prescription used for the GDR parameters. We include the GDR parameters from RT, WFHZ, and the defaults from the STAPRE code. Note that the three of the four prescriptions represented include only a single resonance, whereas in our systematic we include two resonances. The reaction rates are not terribly sensitive to the GDR parameters (or, for that matter, the number of dipole resonances included). The largest changes in the rates are only on the order of 4%, obtained when using the STAPRE defaults.

5.2.5. Width Fluctuation Correction

The final set of panels in Figure **??** show the effect of the WFC the capture reaction rates. The percent change in the value of the rates when the WFC is turned off represents an enhancement of the capture cross section of up to 7-12%.

5.3. Cumulative Uncertainties

Based on the results of the previous sections, we provide an estimate of the total uncertainties in our calculated capture reaction rates. We present two ranges of uncertainty, corresponding to the two categories of sensitivity studies.

The first range of uncertainty represents the uncertainties due to systematic parameters only

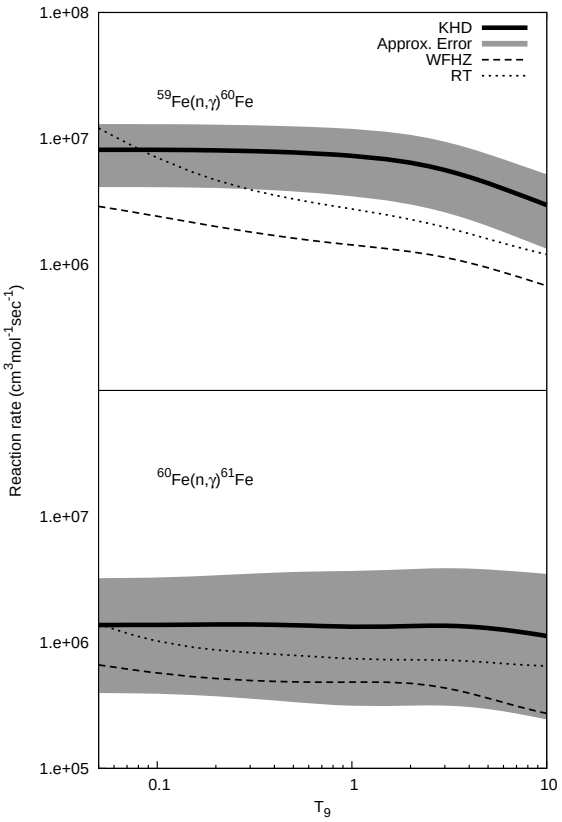

Fig. 11.— Net uncertainty in capture reaction rates based on uncertainties in local systematics

(level density parameter, GDR parameters, and radiation widths), illustrated in Figure 11. Also shown for reference are the reaction rates calculated from the CRSEC and NON-SMOKER codes. The range of uncertainty is +60-75% to -49-55% for ^{59}Fe(n,γ)^{60}Fe and +135-210% to -71-78% for ^{60}Fe(n,γ)^{61}Fe. This range should provide a reasonable estimate of the total uncertainty in these reaction rates. We must stress however that this range of uncertainty does not represent by any means an absolute error in our calculation.

The second range of uncertainty represents all possible combinations of the input quantities for level density prescription (and corresponding set of discrete levels), optical model, inclusion of width fluctuation corrections, GDR parameter prescription, photon strength function prescription, and the approximate systematic errors on the average s-wave photon width to which the photon transmission coefficients were normalized. This

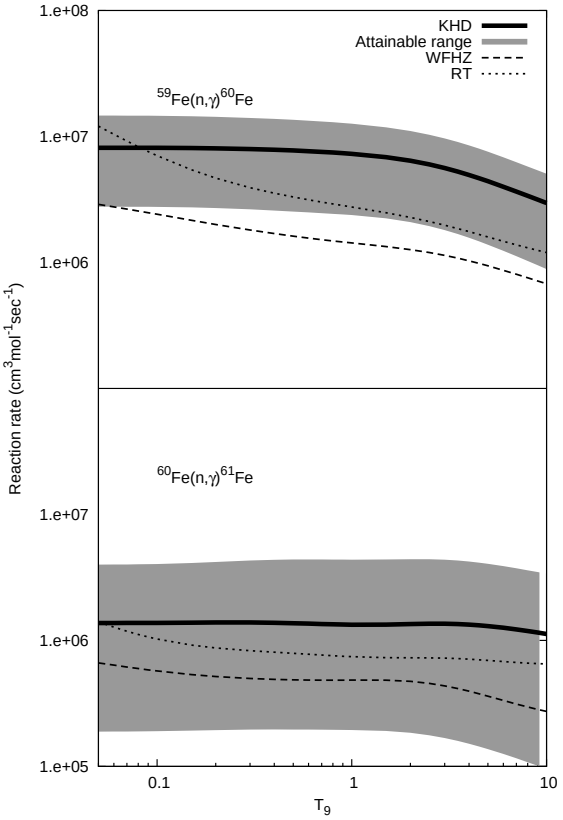

Fig. 12.— Range in capture reaction rates attainable by varying input parameter prescriptions

range is illustrated in Figure 12. The range of uncertainty is +70-80% to -66-70% for ^{59}Fe(n,γ)^{60}Fe and +190-230% to -85-92% for ^{60}Fe(n,γ)^{61}Fe. We note that some of the prescriptions this second range utilize a more limited set of measured data and in some cases represent simpler models of Hauser-Feshbach input quantites. As such, this second uncertainty range should not be interpreted as an "error bar" for the reaction rate, but simply a demonstration of the range that can be attained by varying input quantity prescriptions.

As suggested in Figures 11 and 12, our calculated capture cross sections for both ^{59}Fe and ^{60}Fe targets are always higher than either WFHZ or RT, but are closer to those of RT.

6. Parameterized Single-Zone Nucleosynthesis

We now investigate the effect our newly evaluated ^{59}Fe(n,γ)^{60}Fe and ^{60}Fe(n,γ)^{61}Fe rates will have on the production of ^{60}Fe. These two rates may also indirectly affect the abundances of ^{26}Al, since they can affect the number density of neutrons. We simulate stellar environments using a single zone nucleosynthesis code with an appropriate choice of thermodynamic parameters.

Our calculations include hydrostatic and explosive nucleosynthesis in several nuclear burning stages. In the hydrostatic calculations, the temperature and pressure are kept constant and the burn continues until the primary nuclear fuel is spent. Explosive nucleosynthesis is modeled beginning with a peak density and temperature (ρ_p, T_{9p}) which subsequently decrease as the ejecta cools. The time dependence of the thermodynamic quantites are characterized by a hydrodynamic time scale τ_{HD}:

$$\begin{aligned} \rho(t) &= \rho_p \exp(-t/\tau_{HD}) \\ T_9(t) &= T_{9p} \exp(-t/\tau_{HD}) \\ \tau_{HD} &\approx \frac{1}{\sqrt{24\pi G \rho_0}} = \frac{466}{\sqrt{\rho_0}}. \end{aligned} \tag{38}$$

In both cases, the thermodynamic conditions chosen are representative of those typically found in massive stars, and are identical to those used in (Woosley 1986).

In our analysis, we use our modeled laboratory reaction rates (section 4) as opposed to so-called "stellar rates" which account for the thermal population of excited states in the target nuclei. The differences between the laboratory and stellar rates are often summarized in the form of stellar enhancement factors (SEF), defined as

$$\mathrm{SEF}(T_9) = \frac{\text{Laboratory rate}}{\text{Stellar rate}}. \tag{39}$$

In previous reaction rate calculations, the SEF for neutron capture onto ^{59,60}Fe were generally close to unity for temperatures below $T_9 = 3.0$, as indicated in Table 4. Since our analysis is limited to temperatures lower than $T9 = 3.0$, using laboratory rates in lieu of stellar rates will introduce minor errors into the calculated abundances, generally on the order of 10-25% for ^{60}Fe.

Table 4: Stellar enhancement factors for ^{59}Fe(n,γ)^{60}Fe and ^{60}Fe(n,γ)^{61}Fe

CRSEC		
T_9	^{59}Fe(n,γ)^{60}Fe	^{60}Fe(n,γ)^{61}Fe
0.1	1.000	1.000
0.2	1.000	1.000
0.5	0.999	1.000
1.0	0.983	1.006
2.0	0.879	1.050
3.0	0.784	1.016
4.0	0.738	0.965
NON-SMOKER		
T_9	^{59}Fe(n,γ)^{60}Fe	^{60}Fe(n,γ)^{61}Fe
0.1	1.000	1.000
0.2	1.000	1.000
0.5	1.000	1.000
1.0	0.985	1.000
2.0	0.880	0.996
3.0	0.796	0.986
4.0	0.754	0.992

We have modeled nucleosynthesis using four sets of reaction rates. The first set (A) is the reaction rate library used in the 1995 GCE study. The second rate set (B) is identical to the first, except that we substitute in our laboratory rates for the ^{59}Fe(n,γ)^{60}Fe and ^{60}Fe(n,γ)^{61}Fe reactions (Figure 7). The third set (C) is similar to the second set, except we use the upper limits of the rates as seen in Figure 11. The fourth set (D) uses the lower limits of these rates. The calculations include the network of 336 isotopes presented in table 5.

In previous nucleosynthesis studies, ^{60}Fe was produced primarily in the neon burning shells. In more advanced burning stages, the isotope was destroyed. Thus, we focus our calculations on nuclear processing up through neon burning only.

Hydrostatic Hydrogen Burning

We begin with thermodynamic conditions typical of a hydrogen envelope. The nuclear fuel is processed hydrostatically at a temperature of 0.03×10^9 K and a pressure of 5 g/cm^3. The initial composition of the star is 70.6% ^{1}H and 27.5% ^{4}He, plus solar seeds from (Anders & Grevesse 1989). The burn is allowed to continue until the mass fraction of hydrogen drops below 10^{-5}. The resulting abundances of ^{26}Al and ^{60}Fe are small ($\sim 10^{-11}$ and $\sim 10^{-44}$, respectively)

Table 5: Isotopes included in reaction networks

Element	Masses	Element	Masses
H	1-3	Sc	40-51
He	3-4	Ti	42-52
Li	6-7	V	44-53
Be	7-9	Cr	46-56
B	9-11	Mn	48-57
C	11-14	Fe	50-62
N	13-17	Co	53-65
O	14-20	Ni	56-68
F	17-21	Cu	61-71
Ne	18-24	Zn	64-74
Na	20-25	Ga	67-75
Mg	22-28	Ge	68-76
Al	24-29	As	71-79
Si	26-34	Se	72-82
P	28-35	Br	75-85
S	30-38	Kr	76-88
Cl	33-39	Rb	81-89
Ar	34-42	Sr	82-90
K	36-43	Y	87-91
Ca	38-50	Zr	90-98

The ^{59}Fe(n,γ)^{60}Fe and ^{60}Fe(n,γ)^{61}Fe rates have no significant effect on the ^{26}Al abundances at this stage. Abundances of both nuclides are negligible.

Hydrostatic Helium Burning

Following the depletion of hydrogen, we simulate a helium burning shell. We first explore hydrostatic burning. Typical thermodynamic conditions for this nuclear burning stage consist of a temperature of 0.2×10^9 K and a pressure of 10^3 g/cm^3. For the initial composition of the helium shell, we take the ashes of the previous respective hydrogen burning, i.e. set A uses the ashes of set A hydrogen burning, set B uses the ashes of set B hydrogren burning, etc....

The hydrostatic evolution is allowed to proceed until the helium is depleted to a mass fraction less than 10^{-5}. The resulting mass fractions of ^{26}Al and ^{60}Fe are again comparatively small ($\sim 10^{-19}$ for ^{26}Al and $\sim 10^{-10}$ for ^{60}Fe) , and varying the ^{59}Fe(n,γ)^{60}Fe and ^{60}Fe(n,γ)^{61}Fe rates has a negligible effect on the production of ^{26}Al.

Table 6: ^{26}Al and ^{60}Fe from explosive helium burning

^{26}Al Mass Fraction				
Set	$T_9 = 1.0$	$T_9 = 1.5$	$T_9 = 2.0$	$T_9 = 2.5$
A	7.122×10^{-4}	8.224×10^{-11}	4.606×10^{-11}	1.522×10^{-11}
B	7.122×10^{-4}	8.276×10^{-11}	4.766×10^{-11}	1.541×10^{-11}
C	7.122×10^{-4}	8.270×10^{-11}	4.840×10^{-11}	1.543×10^{-11}
D	7.122×10^{-4}	8.255×10^{-11}	4.537×10^{-11}	1.528×10^{-11}
^{60}Fe Mass Fraction				
Set	$T_9 = 1.0$	$T_9 = 1.5$	$T_9 = 2.0$	$T_9 = 2.5$
A	1.717×10^{-9}	2.119×10^{-4}	1.422×10^{-19}	8.084×10^{-25}
B	8.887×10^{-9}	1.154×10^{-4}	1.027×10^{-19}	7.180×10^{-25}
C	1.390×10^{-8}	3.698×10^{-5}	1.206×10^{-19}	7.155×10^{-25}
D	4.421×10^{-9}	2.845×10^{-4}	1.766×10^{-19}	8.391×10^{-25}

Explosive Helium Burning

Although ^{26}Al and ^{60}Fe are not abundantly produced during hydrostatic helium burning, they can be made explosively. As explained previously, we simulate explosive conditions in our single zone calculations via the time dependence of the temperature and density, which are assumed to have initial peak values as the shock enters the shell and subsequently reduce exponentially. We investigate a range of peak temperatures from $T_9 = 1$ to $T_9 = 2.5$, as suggested in (Woosley 1986). We assume a peak density of 10^4 g/cm^3. The initial composition consists of the ashes of hydrogen burning. The evolution is allowed to continue until the temperature drops below $T_9 = 0.1$

The resulting abundances of ^{26}Al and ^{60}Fe are shown in table 6. We note that ^{26}Al is produced in greatest amounts at $T_9 = 1.0$. ^{60}Fe is produced in greatest abundance at $T_9 = 1.5$. The production of ^{26}Al is not affected by the ^{59}Fe(n,γ)^{60}Fe and ^{60}Fe(n,γ)^{61}Fe rates. Set B results in ^{60}Fe abundances that are roughly a factor of two smaller that those of set A. Using the upper and lower values of our rates results in lower and higher abundances, respectively, possibly suggesting that at this stage of nuclear burning the destruction reaction out of ^{60}Fe is significant (i.e. there is a greater production of ^{60}Fe, but an ever greater depletion of ^{60}Fe via ^{60}Fe(n,γ)^{61}Fe).

Hydrostatic Carbon Burning

In our analysis, we consider a range of temperatures for hydrostatic carbon burning from $T_9 = 1.2$ to $T_9 = 2.2$. The evolution continues until the mass fraction of ^{12}C drops below 10^{-3}. We assume a density of 10^5 g/cm^3 in all cases. Initial compositions are the ashes of the respective hydrostatic helium burning. The results are summarized in Table 7.

The ^{26}Al abundances now show some sensitivity to the choice of ^{59}Fe(n,γ)^{60}Fe and ^{60}Fe(n,γ)^{61}Fe rates, but remain quite similar for each set. Our recommended rates continue to result in lower abundances of ^{60}Fe at $T_9 = 1.5$, although not to the extent seen in explosive helium burning. Again we note that the rate sets using the upper limits of uncertainty in our calculated ^{59}Fe(n,γ)^{60}Fe and ^{60}Fe(n,γ)^{61}Fe rates result in smaller abundances of ^{60}Fe, while the lower rates result in larger abundances.

Explosive Carbon Burning

Any significant amount of ^{60}Fe produced in our hydrostatic carbon burning calculations was made within the first few seconds, and we can therefore expect that the abundances of ^{60}Fe produced in explosive carbon burning will be similar to those in the hydrostatic case. For these explosive calculations, we use the ashes of helium burning as our initial composition. We consider peak temperatures ranging from $T_9 = 1.6$ to $T_9 = 2.2$, with the peak density being 10^5 g/cm^3 in all cases. The evolution continues until the temperature drops to $T_9 = 0.1$. Results are given in Table 8.

Again, we see no significant change in ^{26}Al abundances when the ^{59,60}Fe neutron capture

Table 7: ^{26}Al and ^{60}Fe from hydrostatic carbon burning

^{26}Al Mass Fraction						
Set	$T_9 = 1.2$	$T_9 = 1.4$	$T_9 = 1.6$	$T_9 = 1.8$	$T_9 = 2.0$	$T_9 = 2.2$
A	3.94×10^{-10}	3.10×10^{-8}	9.11×10^{-6}	6.52×10^{-5}	1.71×10^{-5}	6.15×10^{-7}
B	4.14×10^{-10}	3.09×10^{-8}	9.08×10^{-6}	6.75×10^{-5}	1.84×10^{-5}	7.17×10^{-7}
C	3.55×10^{-10}	3.14×10^{-8}	9.10×10^{-6}	7.03×10^{-5}	1.90×10^{-5}	6.86×10^{-7}
D	3.77×10^{-10}	3.12×10^{-8}	9.17×10^{-6}	6.51×10^{-5}	1.88×10^{-5}	7.06×10^{-7}
^{60}Fe Mass Fraction						
Set	$T_9 = 1.2$	$T_9 = 1.4$	$T_9 = 1.6$	$T_9 = 1.8$	$T_9 = 2.0$	$T_9 = 2.2$
A	2.64×10^{-6}	2.35×10^{-4}	4.70×10^{-4}	5.81×10^{-4}	4.12×10^{-4}	1.49×10^{-4}
B	2.12×10^{-6}	1.02×10^{-4}	3.16×10^{-4}	4.51×10^{-4}	3.77×10^{-4}	1.11×10^{-4}
C	4.84×10^{-7}	2.80×10^{-5}	2.37×10^{-4}	3.85×10^{-4}	3.52×10^{-4}	8.49×10^{-5}
D	3.65×10^{-6}	3.11×10^{-4}	5.84×10^{-4}	6.51×10^{-4}	4.46×10^{-4}	1.40×10^{-4}

Table 8: ^{26}Al and ^{60}Fe from explosive carbon burning

^{26}Al Mass Fraction				
Set	$T_9 = 1.6$	$T_9 = 1.8$	$T_9 = 2.0$	$T_9 = 2.2$
A	2.450×10^{-6}	2.823×10^{-6}	6.205×10^{-5}	2.070×10^{-4}
B	2.464×10^{-6}	3.090×10^{-6}	6.253×10^{-5}	2.073×10^{-4}
C	2.490×10^{-6}	3.215×10^{-6}	6.297×10^{-5}	2.074×10^{-4}
D	2.457×10^{-6}	2.904×10^{-6}	6.179×10^{-5}	2.071×10^{-4}
^{60}Fe Mass Fraction				
Set	$T_9 = 1.6$	$T_9 = 1.8$	$T_9 = 2.0$	$T_9 = 2.2$
A	1.276×10^{-6}	1.806×10^{-4}	6.987×10^{-4}	7.397×10^{-4}
B	6.239×10^{-6}	2.907×10^{-4}	6.926×10^{-4}	7.527×10^{-4}
C	8.823×10^{-6}	1.870×10^{-4}	6.447×10^{-4}	7.406×10^{-4}
D	3.338×10^{-6}	3.249×10^{-4}	8.292×10^{-4}	7.925×10^{-4}

rates are modified. In the previous burning stages, our recommended rates generally led to smaller ^{60}Fe abundances. In explosive carbon burning, this is no longer be the case. Using our rates at the lower temperatures results in more ^{60}Fe by a factor of 2-3. For the two higher temperatures, ^{60}Fe abundaces are similar for sets A and B.

In the previous stages, the lower cross sections (set D) resulted in greater abundances of ^{60}Fe and vice versa. The $T_9 = 1.6$ abundances in Table 8 show an opposite effect: the higher cross sections result in greater abundances, perhaps indicating that the destruction of ^{60}Fe by neutron capture does not play as large a role.

We note furthermore that in previous studies ^{60}Fe was produced primarily in the neon burning shell (Timmes *et al.* 1995), while in our calculations ^{60}Fe is being produced abundantly in thermodynamic conditions typical of carbon burning.

Hydrostatic Neon Burning

For hydrostatic neon burning, we consider temperatures ranging from $T_9 = 1.3$ to $T_9 = 2.5$, and a density of 3×10^5 g/cm^3. Initial compositions are the respective ashes of hydrostatic carbon burning at $T_9 = 1.8$. The composition evolves until the mass fraction of ^{20}Ne drops below 10^{-3}. Typical timescales for this evolution range from 10^{10} seconds to 10^{-2} seconds, with the longer times associated with the lower temperatures. Varying only the the ^{59}Fe(n,γ)^{60}Fe and ^{60}Fe(n,γ)^{61}Fe rates changes the evolution time by only $\sim$5%.

The abundances of ^{26}Al and ^{60}Fe following hydrostatic neon burning are shown in Table 9. The

^{26}Al abundances become significant at $T_9 = 2.0$. while ^{60}Fe abundances become large around $T_9 = 1.7$. For $T_9 > 1.5$ the ^{60}Fe abundances are similar to those of the initial compositions (see Table 7), possibly indicating that the abundance of ^{60}Fe does not change much during the course of neon burning.

Explosive Neon Burning

For explosive neon burning, we consider peak temperatures ranging from $T_9 = 1.8$ to $T_9 = 3.2$. In massive stars, the entropy in the convective neon burning shell is roughly constant prior to and after the shock. This condition results in a relationship between the peak temperature and density, where $\rho_p = 4 \times 10^4$ {g/cm^{3}K^{27}) T_{9p}^3 (Woosley & Weaver 1980). Initial compositions are the same as those for hydrostatic neon burning. The mass fractions of ^{26}Al and ^{60}Fe resulting from these explosive runs are summarized in Table 10.

While ^{26}Al is being produced at lower temperatures (compare to the initial compositions in Table 7, ^{60}Fe abundances remain essentially unmodified up to temperature of $T_9 = 2.4$. Above $T_9 = 2.4$, the ^{60}Fe is depleted.

A Result From KEPLER

The process of parameterizing the thermodynamic conditions allows us to study the direct effects of the rates on nucleosynthesis. However, there are aspects of stellar environments that may affect the production of a given isotope which are not accounted for in a single zone calculation. For instance, we have seen that the initial composition can have a significant impact on the nucleosynthesis. In a true stellar model, convection may carry stellar matter from one zone to another, which could result in a continuous supply of, say perhaps, new ^{58}Fe nuclei to seed the production of ^{60}Fe.

Stan Woosley has used our recommended capture rates, along with their upper and lower uncertainties, and modeled the production of ^{60}Fe using the stellar evolution code KEPLER (**?**). The case chosen was a 25 $M_\odot$ star, which in previous studies had produced large amounts of ^{60}Fe. Using the unmodified WFHZ rate set, this particular star produced a total of 2.61×10^{-4} $M_\odot$ of ^{60}Fe. Using our recommended rates, the same star produces 1.86×10^{-4} $M_\odot$ of ^{60}Fe – a factor of 1.4 reduction. This is consistent with our single zone results. The upper and lower limits of our recommended rates produce 2.85×10^{-4} and 2.27×10^{-4} $M_\odot$, respectively. Such non-monotonic behavior is likely due to the fact that raising the rates will increase both the production and destruction of the isotope. This also is consistent with the results in Figure **??** for carbon burning around $T_9 = 1.4$.

The range in ^{60}Fe abundances resulting from modification of the ^{59}Fe(n,γ)^{60}Fe and ^{60}Fe(n,γ)^{61}Fe capture rates is again too small to account for the discrepancy between the predicted and observed flux ratios. It appears likely that other aspects of nucleosynthesis, be it other reaction rates or stellar structure, will have a greater impact on the ^{60}Fe abundance.

7. Conclusions

We have modeled neutron capture cross sections on several isotopes in the region of chromium through zinc. The aim of this modeling effort was to produce reaction rates for neutron capture onto unstable ^{59}Fe and ^{60}Fe targets, which rates are key nuclear uncertainties in the stellar nucleosynthesis of ^{60}Fe. In the process of modeling these rates, we have developed local systematics for the level density parameter and average total S-wave radiation widths. We have used modern prescriptions for our statistical model inputs, including gamma ray strength functions and transmission coefficients. To the greatest extent possible, we have tied these input quantities to measured data. The overall comparison of our modeled cross sections to measured cross section data is superb. Our modeled rates for the ^{59}Fe(n,γ)^{60}Fe and ^{60}Fe(n,γ)^{61}Fe are both higher than those of previous efforts. We have also investigated the sensitivity of our statistical model calculations to uncertainties in the input quantities. This leads us to suggest a likely range of uncertainty in our calculated reaction rates.

We have performed initial nucleosynthesis calculations using a parameterized single zone model. While our new rates tend to produce less ^{60}Fe for most temperatures in various nuclear burning stages, the results are generally well within a factor of two. The abundances change when we use

Table 9: ^{26}Al and ^{60}Fe from hydrostatic neon burning

^{26}Al Mass Fraction						
Set	$T_9 = 1.3$	$T_9 = 1.5$	$T_9 = 1.7$	$T_9 = 2.0$	$T_9 = 2.3$	$T_9 = 2.5$
A	5.00×10^{-13}	7.24×10^{-10}	3.39×10^{-7}	7.51×10^{-5}	5.99×10^{-5}	4.35×10^{-5}
B	4.80×10^{-13}	7.48×10^{-10}	3.37×10^{-7}	7.69×10^{-5}	6.34×10^{-5}	4.47×10^{-5}
C	5.09×10^{-13}	7.32×10^{-10}	3.30×10^{-7}	7.36×10^{-5}	6.01×10^{-5}	4.62×10^{-5}
D	4.90×10^{-13}	7.62×10^{-10}	3.36×10^{-7}	7.51×10^{-5}	6.23×10^{-5}	4.41×10^{-5}
^{60}Fe Mass Fraction						
Set	$T_9 = 1.3$	$T_9 = 1.5$	$T_9 = 1.7$	$T_9 = 2.0$	$T_9 = 2.3$	$T_9 = 2.5$
A	1.52×10^{-16}	1.27×10^{-13}	3.07×10^{-4}	5.48×10^{-4}	4.99×10^{-4}	4.38×10^{-4}
B	7.20×10^{-17}	7.19×10^{-14}	2.37×10^{-4}	4.22×10^{-4}	3.68×10^{-4}	2.91×10^{-4}
C	6.42×10^{-17}	6.66×10^{-14}	2.00×10^{-4}	3.57×10^{-4}	2.99×10^{-4}	2.19×10^{-4}
D	1.08×10^{-16}	9.83×10^{-14}	3.43×10^{-4}	6.13×10^{-4}	5.50×10^{-4}	4.65×10^{-4}

Table 10: ^{26}Al and ^{60}Fe from explosive neon burning

^{26}Al Mass Fraction								
Set	$T_9 = 1.8$	$T_9 = 2.0$	$T_9 = 2.2$	$T_9 = 2.3$	$T_9 = 2.4$	$T_9 = 2.5$	$T_9 = 2.7$	$T_9 = 2.9$
A	6.50×10^{-5}	6.54×10^{-5}	7.60×10^{-5}	1.04×10^{-4}	1.25×10^{-4}	5.16×10^{-5}	5.65×10^{-7}	6.76×10^{-8}
B	6.73×10^{-5}	6.77×10^{-5}	7.87×10^{-5}	1.07×10^{-4}	1.29×10^{-4}	5.28×10^{-5}	5.67×10^{-7}	6.84×10^{-8}
C	7.01×10^{-5}	7.05×10^{-5}	8.19×10^{-5}	1.11×10^{-4}	1.32×10^{-4}	5.43×10^{-5}	5.68×10^{-7}	6.82×10^{-8}
D	6.49×10^{-5}	6.53×10^{-5}	7.59×10^{-5}	1.04×10^{-4}	1.25×10^{-4}	5.16×10^{-5}	5.93×10^{-7}	6.80×10^{-8}
^{60}Fe Mass Fraction								
Set	$T_9 = 1.8$	$T_9 = 2.0$	$T_9 = 2.2$	$T_9 = 2.3$	$T_9 = 2.4$	$T_9 = 2.5$	$T_9 = 2.7$	$T_9 = 2.9$
A	5.81×10^{-4}	5.81×10^{-4}	5.78×10^{-4}	5.67×10^{-4}	5.26×10^{-4}	4.49×10^{-4}	2.25×10^{-4}	5.17×10^{-7}
B	4.51×10^{-4}	4.51×10^{-4}	4.49×10^{-4}	4.39×10^{-4}	4.00×10^{-4}	3.11×10^{-4}	1.73×10^{-5}	1.99×10^{-10}
C	3.85×10^{-4}	3.85×10^{-4}	3.83×10^{-4}	3.74×10^{-4}	3.36×10^{-4}	2.42×10^{-4}	2.69×10^{-6}	1.47×10^{-10}
D	6.51×10^{-4}	6.51×10^{-4}	6.48×10^{-4}	6.35×10^{-4}	5.86×10^{-4}	4.84×10^{-4}	1.09×10^{-4}	4.09×10^{-10}

the upper and lower uncertainties in our recommended rates, but still they are generally within a factor of two. These results are in agreement with calculations involving more complex stellar models. These calculations suggest that the disparity in the stellar abundance of ^{60}Fe between the 1995 GCE survey and the more recent nucleosynthesis cannot be accounted for by the ^{59}Fe(n,γ)^{60}Fe and ^{60}Fe(n,γ)^{61}Fe reaction rates alone.

8. Acknowledgments

This work was performed under the auspices of the U.S. Department of Energy by the University of California Lawrence Livermore National Laboratory under contract W-7405-ENG-48.

REFERENCES

Anders, E. & Grevesse, N. 1989, Geochim. Cosmochim. Acta, **53**, 197

Bao, Z.Y., Beer, H., Käppler, F., Voss, F., & Wisshak, K. 2000, Atomic Data & Nuclear Data Tables, **76**, 70

Bauer, R. LLNL 2003, private communication.

Blatt, J.M., & Weisskopf, V.F., *Theoretical Nuclear Physics* (Wiley: New York), 1952

Chadwick, M. 1998, "The GNASH statistical model code", http://www.nea.fr/abs/html/psr-0125.html

Cline, C.K., & Blann, M. 1971, Nuc. Phys. **A172**, 225

ENSDF: Evaluated Nuclear Structure Data File, Brookhaven National Laboratory, US Dept. of Energy, http://www.nndc.bnl.gov/nndc/ensdf/

EXFOR: Experimental Nuclear Reaction Data File, Brookhaven National Laboratory, US Dept. of Energy, http://www.nndc.bnl.gov/nndc/exfor/

Gadioli, E., Gadioli Erba, E., Parker, D., & Sona, P.G. 1973, Nuc. Phys. **A217**, 589

Gardner, D.G., "Model Calculations as one Means of Satisfying the Neutron Cross Section Requirements of the CTR Program", NBS Special Publication 425, Washington D.C., March 3-7, 1975

Gilbert, A., & Cameron, A.G.W. 1965, Can. J. Phys., **43**, 1446

Harris, M.J. 2005, A&A **433**, L49

Hauser, W., & Feshbcah, H. 1952, Phys. Rev. **87**, 366

Hoffman, R. D., Woosley, S. E., Weaver, T. A., Rauscher, T., & Thielemann, F.-K. 1999, ApJ, **521**, 735

Hoffman, R. D., Rauscher, T., Heger, A., & Woosley, S. E. 2002, "Reaction Rates for Stellar Nucleosynthesis", http://www-pat.llnl.gov/Research/RRSN/

Hoffman, R.D., Dietrich, F.S., Bauer, R., Kelley, K. & Mustafa, M. "Neutron and Charged-Particle Induced Cross Sections for Radiochemistry in the Region of Bromine and Krypton",UCRL-TR-205563, LLNL, 2004; Hoffman, R.D., Dietrich, F.S., Bauer, R., Kelley, K. & Mustafa, M. "Neutron and Charged-Particle Induced Cross Sections for Radiochemistry in the Region of Iodine and Xenon",UCRL-TR-206721, LLNL, 2004; Hoffman, R.D., Dietrich, F.S., Bauer, R., Kelley, K. & Mustafa, M. "Neutron and Charged-Particle Induced Cross Sections for Radiochemistry in the Region of Samarium, Europium, and Gadolinium",UCRL-TR-211588, LLNL, 2005

Holmes, J. A., Woosley, S. E., Fowler, W. A. & Zimmerman, B. A. 1976, Atomic Data & Nuclear Data Tables, **18**, 305

Iljinov, A.S., Mebel, M.V., Bianchi, N., De Sanctis, E., Guaraldo, C., Lucherini, V., Muccifora, V., Polli, E., Reolon, A.R., & Rossi, P. 1992, Nucl. Phys. **A543**, 517

Jeukenne, J.-P., Lejeune, A., & Mahaux, C. 1977 Phys. Rev. **C16**, 80

Koning, A.J., & Delaroche, J.P. 2003, Nucl. Phys. **A713**, 231

McFadden, L., and Satchler, G.R. 1966, Nuc. Phys. **84**, 177

Michaud, G. & Fowler, W.A. 1970, Phys. Rev. **C2**, 2041

Milazzo-Colli, L., and Braga-Marcazzan, G.M., 1973 Nuc. Phys. **A210**, 297

Moldauer, P.A. 1976 Phys. Rev. **C14** 764

Möller, P., Nix, J.R., Myers, W.D., & Swiatecki, W.J. 1995, Atomic Data & Nuclear Data Tables, **59**, 185

Perey, C.M. and Perey, F.G. 1963, Phys. Rev. **132**, 755

Prantzos, N. 2004, A&A, **420**, 1033

Rauscher, T., Thielemann, F.-K., & Kratz, K.-L. 1997, Phys. Rev. C., **56**, 1613

Rauscher, T., Thielemann, F.-K. 2000, Atomic Data & Nuclear Data Tables, **75**, 1 http://quasar.physik.unibas.ch/~tommy/reaclib.html#REACLIB

Rauscher, T., Thielemann, F.-K. 2001, Atomic Data & Nuclear Data Tables, **79**, 47 (addendum)

Rauscher, T., Heger, A. Hoffman, R. D. & Woosley, S. E. 2002, ApJ, **576**, 323

Raynal, J. "ECIS96", Proceedings of the Specialists' Meeting on the Nucleon Nucleus Optical Model up to 200 MeV, 13-15 November 1996, Bruyeres-le-Chatel, France (http://www.nea.fr/html/science/om200/raynal.pdf)

Reffo, G. 1978, ICTP Lecture Series, 17 Jan. - 10 Mar., Trieste

RIPL: Reference Input Paramete Library, *Handbook for calculations of nuclear reaction data*, 1998, IAEA-TECDOC-1034

Smith, D. M. 2003, ApJL, **589**, L55

Smith, D.M. 2004, in The INTEGRAL Universe, ed. V. Schönfelder, G.G. Licht & C. Winkler (Noordwljki:ESA), ESA Spec. Publ. 552, 45

Timmes, F. X., Woosley, S. E., & Weaver, T. A. 1995, ApJS **98** , 617

Timmes, F. X., Woosley, S. E., Hartmann, D. H., Hoffman, R. D., Weaver, T. A., & Matteucci, F. 1995, ApJ **449**, 204

Uhl, M., & Strohmaier, B. IRK-Vienna Report IRK-76/01 1976 (Upd. 1978)

Voinov, A., et al., 2004, Phys. Rev. Lett. **93**, 142504

A.H. Wapstra, G. Audi, and C. Thibault. 2003, Nuc. Phys. **A729**, 129

Woosley, S.E., "Nucleosynthesis and Stellar Evolution", SAAS-FEE 1986 (Geneva Observatory:Switzerland)

Woosley, S. E., Fowler, W. A., Holmes, J. A. & Zimmerman, B. A. 1975, Orange Aid Preprint OAP-422, Caltech

Woosley, S.E., & Weaver, T.A. 1980, ApJ **238**, 1017

Woosley, S. E., & Weaver, T. A. 1995, ApJS **101**, 181

This 2-column preprint was prepared with the AAS LaTeX macros v5.0.